The Astrophysical Journal, 900:54 (25pp), 2020 September 1 https://doi.org/10.3847/1538-4357/aba1e3
© 2020. The American Astronomical Society. All rights reserved.

Explosive Nucleosynthesis in Near-Chandrasekhar Mass White Dwarf Models for Type Iax Supernovae: Dependence on Model Parameters

Shing-Chi Leung[1,2] and Ken'ichi Nomoto[1]
[1] Kavli Institute for the Physics and Mathematics of the Universe (WPI), The University of Tokyo Institutes for Advanced Study, The University of Tokyo, Kashiwa, Chiba 277-8583, Japan; scleung@caltech.edu
[2] TAPIR, Walter Burke Institute for Theoretical Physics, Mailcode 350-17, Caltech, Pasadena, CA 91125, USA
Received 2019 September 27; revised 2020 June 30; accepted 2020 June 30; published 2020 August 31

Abstract

The recently observed diversity of Type Ia supernovae (SNe Ia) has motivated us to conduct the theoretical modeling of SNe Ia for a wide parameter range. In particular, the origin of Type Iax supernovae (SNe Iax) has been obscure. Following our earlier work on the parameter dependence of SN Ia models, we focus on SNe Iax in the present study. For a model of SNe Iax, we adopt the currently leading model of pure turbulent deflagration of near-Chandrasekhar mass C+O white dwarfs (WDs). We carry out two-dimensional hydrodynamical simulations of the propagation of the deflagration wave, which leaves a small WD remnant behind and ejects nucleosynthesis materials. We show how the explosion properties, such as nucleosynthesis and explosion energy, depend on the model parameters, such as central densities and compositions of the WDs (including the hybrid WDs), turbulent flame prescription, and initial flame geometry. We extract the associated observables in our models and compare with the recently discovered low-mass WDs with unusual surface abundance patterns and the abundance patterns of some SN remnants. We provide the nucleosynthesis yield tables for applications to stellar archeology and galactic chemical evolution. Our results are compared with the representative models in the literature.

Unified Astronomy Thesaurus concepts: Explosive nucleosynthesis (503); Type Ia supernovae (1728); Hydrodynamical simulations (767); White dwarf stars (1799); Supernova remnants (1667)

1. Introduction

Type Ia supernovae (SNe Ia) are important in a cosmological and chemical context. Their standardized light curves with Phillip's relation (Phillips 1993) lead to the use of SNe Ia as standard candles and the discovery of cosmic acceleration and its implications of dark energy (Riess et al. 1996; Perlmutter et al. 1997). The SNe Ia are also the major channel for iron-peak element production (e.g., Nomoto & Leung 2017a). The role of SNe Ia can be seen in the galactic chemical evolution, including the [α/Fe] versus [Fe/H] relation (Nomoto et al. 2013) and the [Mn/Fe] versus [Fe/H] relation (Seitenzahl et al. 2013; Kobayashi et al. 2020; Leung & Nomoto 2020).

The diversified observational properties of SNe Ia (e.g., Li et al. 2001; Foley et al. 2016; Taubenberger 2017; Jiang et al. 2018) suggest multiple explosion mechanisms (see, e.g., García-Berro & Lorén-Aguilar 2017; Hoeflich 2017; Nomoto & Leung 2017a; Pakmor 2017; Röpke 2017, for recent reviews).

In our earlier work with two-dimensional hydrodynamical simulations, we studied the turbulent deflagration model with and without the deflagration–detonation transition (DDT) for the near-Chandrasekhar mass C+O white dwarfs (WDs; Leung & Nomoto 2018) and the double detonation (DD) models for both sub-Chandrasekhar mass WDs and near-Chandrasekhar mass WDs (Leung & Nomoto 2020). We have shown how the explosion properties, such as nucleosynthesis, explosion energy, and asphericity, depend on the model parameters of the flame and WDs.

In the present work, we focus on Type Iax supernovae (SNe Iax; e.g., Jha 2017, for a review). A few well-observed SNe Iax are SN 2002cx (e.g., Li et al. 2003), SN 2005hk (e.g., Phillips et al. 2007), SN 2008 ha (e.g., Foley et al. 2009) and SN 2014dt (Kawabata et al. 2018). The SNe Iax are peculiar SNe Ia, having lower luminosities, as well as lower ejecta velocities and masses, than normal SNe Ia. Moreover, SNe Iax show quite a large variation of light-curve and ejecta properties. The SNe Iax are peculiar but may not be rare, as indicated by their statistics. They contribute $\sim$10% of the SN Ia population (Li et al. 2001).

Among the various proposed models, we adopt a pure deflagration model, which has been shown to be a promising model to explain the main properties of SNe Iax (e.g., Branch et al. 2004; Phillips et al. 2007; Sahu et al. 2008; Foley et al. 2009; Jordan et al. 2012; Kromer et al. 2013; Fink et al. 2014). The outcome of the pure deflagration depends mainly on the subsonic flame speed (e.g., Nomoto et al. 1976, 1984; Gamezo et al. 2004; Röpke et al. 2007; Jordan et al. 2012; Fink et al. 2014), and the weak explosions with low kinetic energy and small production of ^{56}Ni can be consistent with the observed properties of SNe Iax.

In our earlier works on the hydrodynamics and nucleosynthesis of SNe Ia (Leung & Nomoto 2018, 2020), we showed that the abundance patterns of nucleosynthesis yields are important to constrain the SN model from the light curves and spectra. In the present study, we perform two-dimensional simulations of pure turbulent deflagration (PTD) and calculate nucleosynthesis for near-Chandrasekhar mass WDs with various parameters, such as the composition (C+O and C+O+Ne) and central densities of WDs, and flame physics, such as initial flame geometry.

We provide tables of our nucleosynthesis yields and compare them with the unusual abundance patterns of some WDs and SN remnants (SNRs) to infer their origins. Our results could be important to the chemical evolution of some dwarf spheroidal galaxies (dSphs). In Kobayashi et al. (2015), the SN Iax model can be an explanation for the early drop in [O/Fe] and early rise in [Mn/Fe] relations.

In Section 2, we describe the progenitor stars and WDs and briefly review the methods and input physics to calculate the PTD. In Section 3, we present typical hydrodynamical and thermodynamical properties of the PTD models. We investigate how the chemical yields of SNe Iax change with the model parameters. We compare our yields with some metal-enriched low-mass WDs and SNRs and discuss their application to the chemical evolution of galaxies.

2. Initial Models and Input Physics

2.1. Initial Models

We first construct an isothermal WD in hydrostatic equilibrium with a central density ρ_c, temperature $T_{\rm ini}$, and metallicity Z. In the equation of state, Coulomb effects are taken into account. The characteristic model described in the next section assumes a C+O WD of mass 1.37 $M_\odot$ with a central density of $3 \times 10^9\,{\rm g\,cm^{-3}}$ and solar metallicity. In the simulation solar metallicity is represented by the characteristic isotope ^{22}Ne with the mass fraction of $X(^{22}{\rm Ne}) = 0.025$ (Nomoto 1984; Leung & Nomoto 2018). The composition is different from the detailed solar composition (Asplund et al. 2009). However, we remark that the nucleosynthesis results are insensitive to the exact representation because the nucleosynthesis depends primarily on the electron mole fraction $Y_{\rm e}$ of the burnt matter, which is dominated by electron capture after the matter is swept by the deflagration wave. The initial electron mole fraction and composition play much smaller roles unlike the canonical deflagration with deflagration-detonation transition due to the lack of nucleosynthesis by detonation at low densities.

Such a C+O WD is assumed to be formed in the single degenerate channel of binary evolution (e.g., Nomoto 1982a; Nomoto & Leung 2017a, 2018). Thus, the central density of the WD mainly depends on the accretion rate. It also depends on the spin of the WD (e.g., Benvenuto et al. 2015) for which the central density at the deflagration is as high as (5–6) $\times 10^9\,{\rm g\,cm^{-3}}$ and even higher, depending on the timescale of the angular momentum loss. Thus, we parameterized the central density.

We also consider possible hybrid WDs, as demonstrated by Denissenkov et al. (2013). Here carbon is ignited in the outer layer of the C+O core of a nearly $\sim$10 $M_\odot$ star during its asymptotic giant branch (AGB) phase (e.g., Nomoto 1984). If the carbon flame propagates through the center, the C+O core is converted into an O+Ne+Mg core (e.g., Nomoto 1987; Nomoto & Leung 2017b). However, if the overshooting of convection across the carbon flame down to the C+O layer is large, it would reduce the nuclear fuel to prevent the carbon flame from propagation to the center (however, see, e.g., Lecoanet et al. 2016; Brooks et al. 2017). Then the degenerate core is composed of C+O in the central region and O+Ne+Mg in the outer layer, where the composition changes at a designed transition mass $M_{\rm core}$.

When such a core becomes a WD, it is called a hybrid WD. When the mass of the hybrid WD becomes close to the near-Chandrasekhar limit, carbon is ignited in the central region, which produces a convection zone. During the simmering phase, the convection mixes the central C+O core and the outer O+Ne+Mg layer before the deflagration is initiated. It produces a WD made of a C+O+Ne mixture.

In the present study, we assume that such a hybrid WD is formed and the C+O-rich core is completely mixed with the outer O+Ne-rich envelope for simplicity. After mixing during the simmering phase, we assume that the WD has a uniform composition where the mass fractions of ^{12}C, ^{16}O, and ^{20}Ne are 0.2, 0.5, and 0.3 for simplicity (Kromer et al. 2015) and in view of the uncertainties in the overshooting parameter. The effect of metallicity is included by combining the above composition with ^{22}Ne as the key isotope for metallicity.

If the carbon burning reaches the center, the WD becomes an O+Ne+Mg WD. These WDs undergo electron capture and are very likely to collapse to form neutron stars (Suzuki et al. 2019; Leung et al. 2019; Zha et al. 2019). For a possible case of partial mass ejection, the nucleosynthesis yields are given in Appendix C.

2.2. Methods and Input Physics

For the adopted initial models of the WDs, we perform two-dimensional hydrodynamics simulations of the propagation of the PTD by specifying the initial deflagration structure.

Deflagration (Nomoto et al. 1976; Nomoto 1982b; Timmes & Woosley 1992; Niemeyer & Woosley 1997; Woosley 1997) is the nuclear flame, where thermonuclear runaway takes place with a timescale shorter than the dynamical timescale. The flame propagates at a subsonic speed by energy transport across the flame due to electron conduction and convection, as described below (e.g., Leung & Nomoto 2017b, 2019; Nomoto & Leung 2017a, 2017b; Leung et al. 2020).

Deflagration is subject to hydrodynamical instabilities, including the Rayleigh–Taylor (RT), Kelvin–Helmholtz (KH), and Landau–Darrieus (LD) instabilities present during its propagation (e.g., Timmes 1992; Livne & Arnett 1993; Niemeyer & Hillebrandt 1995; Bell et al. 2004a, 2004b; Röpke et al. 2004a, 2004b). The flame width ($\sim 10^{-6}$–10^{-3} cm) is generally much smaller than that resolved by simulation (e.g., Timmes & Woosley 1992; Niemeyer et al. 1995). A special flame front tracking technique, such as the level-set method (Osher & Sethian 1988), is necessary for a consistent description of the interaction between the flame and the dynamics (Reinecke et al. 1999b). A subgrid-scale turbulence model is often necessary (Clement 1993; Schmidt et al. 2006). The flame structure is coupled with turbulence, where the turbulent motion emerges in the length scale down to the Kolmogorov scale. Eddy motions can alter the deflagration front by fluid advection above the Gibson's scale. Below that scale, the irregularities are polished (e.g., Niemeyer et al. 1995; Jackson et al. 2014). Early multidimensional realizations were done in, e.g., Reinecke et al. (1999a, 2002a, 2002b), Röpke et al. (2004a, 2004b), Röpke & Hillebrandt (2005), Röpke (2005), and Röpke et al. (2006a, 2006b).

The turbulent deflagration is tracked by the level-set method (Osher & Sethian 1988; Reinecke et al. 1999b) with the subgrid turbulence scheme given in Clement (1993) and Niemeyer et al. (1995). The turbulent flame formula used the analytical results in Pocheau (1994). The connections between the local turbulence strength and the effective turbulent flame propagation speed are taken from Schmidt et al. (2006) but with variations shown in Hicks (2015). The DDT is artificially suppressed throughout the simulation.

Our simulation code is a general hydrodynamics code embedded with SN physics (Leung et al. 2015). This code has been applied to previous SN Ia parameter surveys for the near-Chandrasekhar mass WDs (Leung & Nomoto 2017a, 2018) and also sub-Chandrasekhar mass WDs (Leung & Nomoto 2020). The code has recently been extended to study other types of SNe, including electron-capture (Leung et al. 2020) and

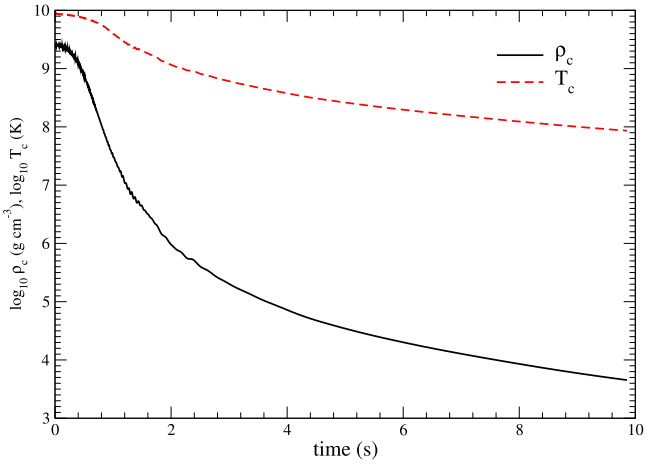

Figure 1. Central density (black solid line) and central temperature (red dashed line) against time for the characteristic model.

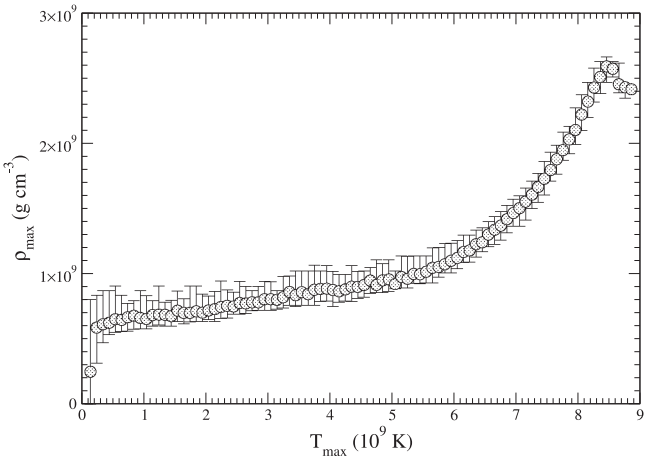

Figure 2. Maximum density against maximum temperature for the characteristic model using the thermodynamics history of the tracer particles. The error bars and data points correspond to the range of density and mean density of the tracer particles obtained in the thermodynamics history.

jet-driven (Tsuruta et al. 2018) SNe. The simulation code uses a simplified seven-isotope network (Timmes et al. 2000) to trace the isotopic abundances and a three-step burning network (Townsley et al. 2002) to mimic the nuclear reactions in deflagration.

In the three-step burning scheme, the fast reaction of carbon burning is controlled by the level-set method. The advanced and O burning are set to be dependent on the corresponding burning timescales (Calder et al. 2007). For matter with a sufficiently high density ($>10^8$ g cm^{-3}) and temperature ($>5 \times 10^9$ K) such that the matter is burned in nuclear statistical equilibrium (NSE), electron captures take place. The corresponding rates for the matter in NSE are computed by summing up the individual rates of many isotopes included in the nuclear reaction network used by the postprocessing. Updated weak interaction rates are obtained from the literature, including Nabi & Klapdor-Kleingrothaus (2004) and Seitenzahl et al. (2009). We refer the reader to Appendix A for further details.

Pure deflagration cannot completely unbind the star if the flame is quenched early by the WD expansion (Nomoto et al. 1976; Livne 1993). Its subsonic nature provides sufficient time for electron capture to take place before the WD expands (e.g., Iwamoto et al. 1999; Seitenzahl et al. 2009), which is a key to producing neutron-rich isotopes in the ejecta. Such conditions are hardly achieved by other types of SNe.

After the hydrodynamical simulations, we use the thermodynamics history of the tracer particles to reconstruct the detailed nucleosynthesis (Travaglio et al. 2004; Seitenzahl et al. 2009; Townsley et al. 2016).

3. Characteristic Model for SNe Iax

We first examine the typical behavior of SNe Iax based on the C+O WD as described in Section 2. Then we examine the stellar properties, thermodynamics, energetics, and chemical properties. A central flame, *c*3 (corresponding to three-finger; see Reinecke et al. 1999a for illustrations), is placed at the beginning.

3.1. Thermodynamics

In Figure 1, we plot the central density (black solid line) and central temperature (red dashed line) of the characteristic model as a function of time. After the core is burned, it remains static for the first 0.2 s. Afterward, it expands, and the central density drops by 2 orders of magnitude in the first 2 s. Then the core expansion slows down. It reaches an asymptotic value of $\sim 10^{4.5}$ g cm^{-3} beyond 8 s, showing that the core stops expanding because it has transferred all its momentum to the outer material, which has a relatively lower density and hence smaller inertia to be ejected. The temperature shows a similar evolution but with a difference that the core temperature continues to drop, even at the end of the simulation. The temperature is too low for any important nuclear reactions to take place after it has left NSE (defined at $T > 5 \times 10^9$ K), which occurs at $\sim$1 s after explosion.

To further clarify the effects of nuclear reactions in the star, we plot in the tracer particle summary Figure 2. In this figure, for each tracer particle, we search for its maximum density and temperature achieved in the simulations, and then we bin them into different temperature ranges. The variety of particle maximum densities within the same temperature range is represented by the error bars in the figure. Notice that for SNe Iax, the maximum ρ_c and T_c are obtained at the same time because there is no shock wave triggered in the event.

There are two groups of particles developed in the simulation. The first group corresponds to the particles that are directly burned; this consists of particles with $\rho_{\max} \gtrsim 6 \times 10^9$ K. There is a monotonic relation between $\rho_{\max}$ and $T_{\max}$, and the fluctuation is very small. The star remains close to static, and the asymmetry of the deflagration wave is not large enough to create a significant time difference for burning matter near the same radius. The second group corresponds to the particles being burned by the deflagration wave but after the star has expanded and the flame becomes aspherical. Matter with the same $\rho_{\max}$ can have different $T_{\max}$. This means that they have the same initial density but experience different levels of expansion before the deflagration arrives.

3.2. Energetics

In Figure 3, we plot the energy production rate against time for the characteristic model. The energy production rate is defined by $\Delta Q/\Delta t$, where ΔQ is the amount of energy gained by the system through nuclear reaction at that current step with a time step size Δt. The amount of energy, as described in

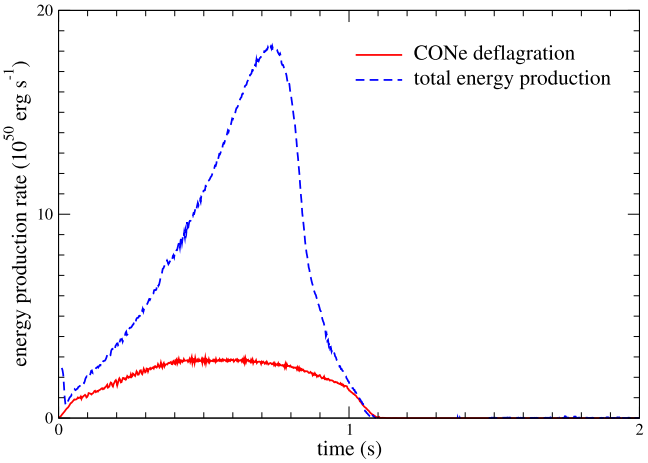

Figure 3. Energy production rate (blue dashed line) and its component (red solid line) against time for the characteristic model. Here the energy production rate by CONe deflagration is extracted for comparison.

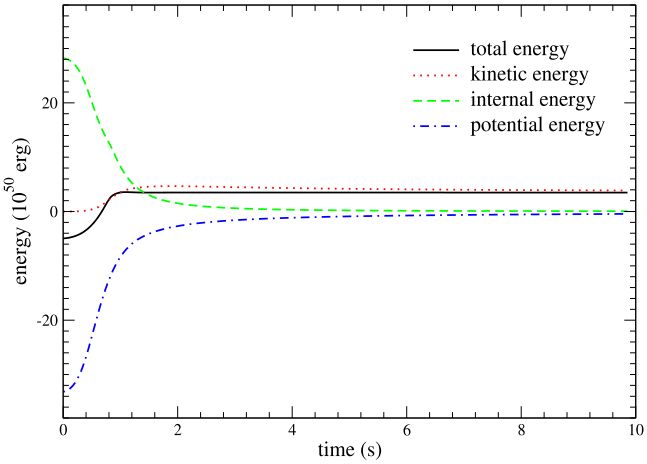

Figure 4. Total (black solid line), kinetic (red dotted line), internal (green dashed line), and gravitational (blue dotted–dashed line) energy against time for the characteristic model.

Section 2, is done by the level-set methods coupled with our simplified network.

In the first 0.4 s, the system releases energy mainly by nuclear deflagration. The energy production rate is low, $\sim 10^{50}$ erg s^{-1}. After that, from 0.4 to 1 s, the energy production switches to advance and NSE burning when the density at the deflagration front becomes low ($\sim 10^{7}$ g cm^{-3}). The energy production rate is high and reaches $\sim 10^{51}$ erg s^{-1} at maximum. At that time, nuclear deflagration no longer produces any observable amount of energy. We remark that, different from standard SNe Ia, there can be enhancement from mixing of fresh ^{16}O and ^{20}Ne into the ash when the ash expands.

In Figure 4, we plot the energy evolution similar to Figure 3. The total, kinetic, internal, and potential energy are plotted.

Similar to the energy production rate, the total energy quickly rises at the beginning and reaches its equilibrium value at $\sim$1 s after the flame has propagated. When the expansion quenches the flame and cools down the ash, the total energy no longer changes. The kinetic energy shows a similar behavior but with a small bump at about 1.3 s. This is because during the expansion of the flame, it creates nonlocal acceleration of matter, especially the hot matter.

The total internal energy, on the contrary, is dominated by the initial internal energy. It constantly decreases, showing that the star expands and loses energy through the expansion work done. Unlike SNe Ia, it has no bump in its evolution, which means that the flame does not produce any significant shock compression to the matter, including the low-density matter on the surface. This is consistent with the idea that the deflagration is subsonic. The system always has sufficient time to adjust its structure to accommodate the energy input by nuclear burning. It reaches its asymptotic energy of $\sim$zero beyond 3 s.

For the gravitational energy, since there is no contraction during the whole evolution, it quickly rises in the first 2 s and then slowly approaches its asymptotic value near zero as the star expands. But it reaches its asymptotic value much slower than the internal energy, showing that the system is expanding much slower than ordinary SNe Ia.

3.3. Flame Propagation

In Figure 5, we plot the flame structure of our representative model from the beginning to 2.5 s at an interval of 0.5 s. We use the $c3$ flame, which we have applied in previous SN Ia surveys. This flame mimics and promotes the early growth of RT instabilities. We note that putting a spherical flame at the center can give enhanced flame propagation along the symmetry axis, while the WD does not have a preferred direction due to its static initial profile. Therefore, to avoid the development of such unphysical structure, we use the $c3$ flame so that the off-axis flame development dominates the growth of the flame.

We also simulate PTD in the hybrid WD, which is composed of C+O+Ne matter. At 0.5 s, the flame only burns the innermost $\sim$200 km of the star. One of the "finger" features near the y-axis is suppressed, while the other two fingers continue to grow further. The curly color pattern in its temperature distribution demonstrates the turbulent motion inside the ash at 1.5 s. At that time, the flame has already cooled down to about $\sim 5 \times 10^{9}$ K. After that, both NSE burning and nuclear deflagration no longer supply extra energy. The star gradually expands. The peak temperature reaches $\sim 3 \times 10^{9}$ K at 2.0 s and $\sim 2 \times 10^{9}$ K at 2.5 s. From 2.0 s onward, when the flame expands upward due to its buoyancy, the unburned matter floats downward to fill up the space. The opposite direction of the flow current creates the KH instability, where the curly structure can be seen along the fingers. On top of the flame, smaller-scale "mushroom" shapes emerge as the RT instabilities. This occurs when the lower-density ash creates a pressure inversion with the higher-density fuel against the gravitational force. Also, the inverse mushroom shape can be seen at the inner part of the ash, showing the injection of fuel into the ash. The color map of the temperature further shows instabilities in the smaller length scale inside the ash.

3.4. Isotopic Abundance

Unlike normal SNe Ia, the low explosion energy means that the star is not completely disrupted by the nuclear flame. At the beginning, the burned matter has the largest momentum that can escape from the star. However, during its upward motion, it transfers part of its momentum to the matter of lower density in the outer part of the star. Part of the burned matter thus becomes bounded during this momentum transfer. Instead, the surface matter is expelled. To clarify which part of the star can be ejected and which part remains bounded in the star, we use the

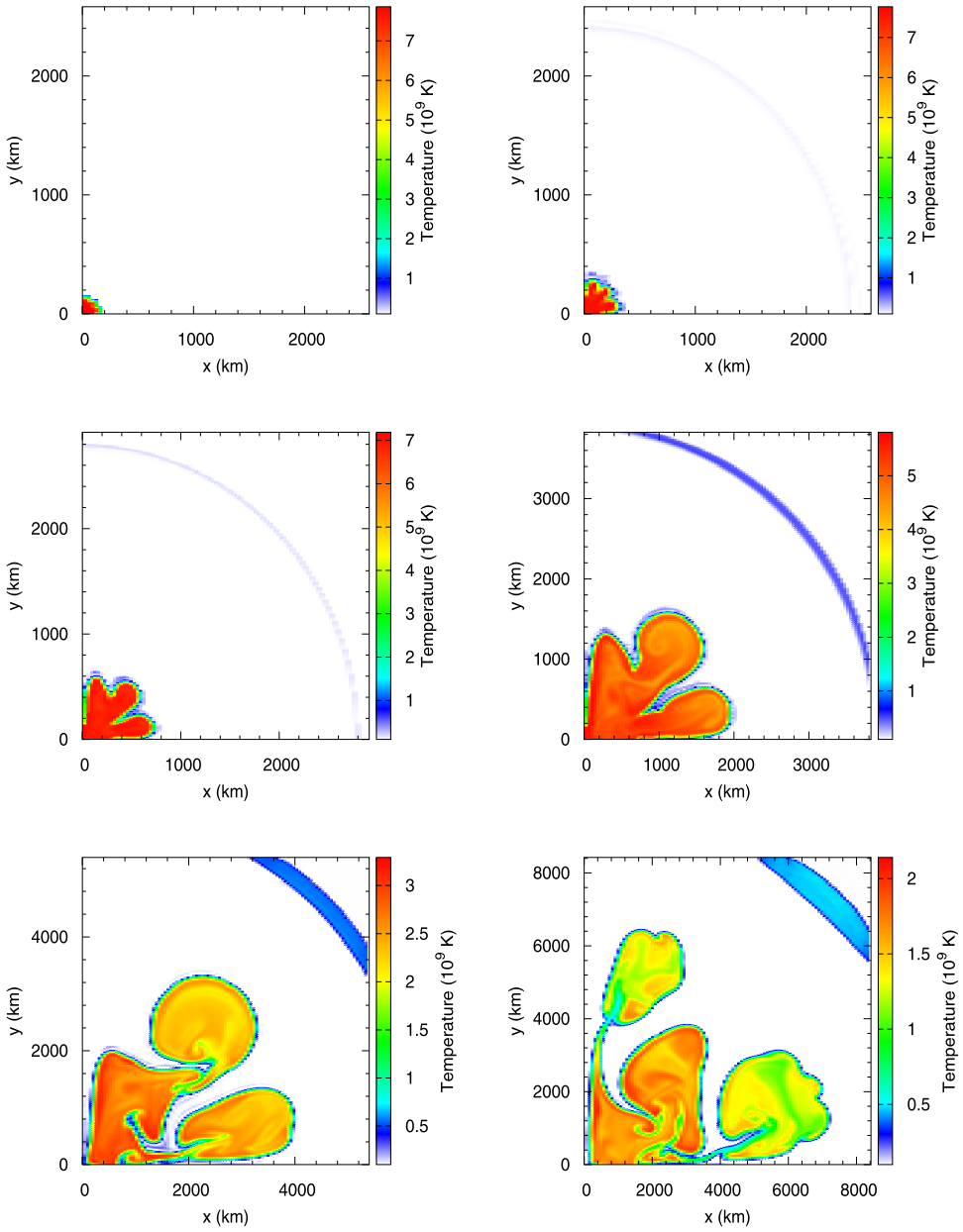

Figure 5. Flame structure and temperature color plots of the characteristic model from the beginning to 2.5 s after deflagration has started at an interval of 0.5 s.

kinematic properties of the tracer particles. For each tracer particle, we obtain its specific kinetic energy $|\boldsymbol{v}|^2/2$ and current gravitational energy $\phi(\boldsymbol{r})$ from the end of the simulations. We assume that tracer particles can escape when $|\boldsymbol{v}|^2/2 + \phi(\boldsymbol{r}) > 0$. We notice that the tracer particles satisfying this relation remain unchanged beyond a few seconds after explosion.

In Figure 6, we plot the tracer particles that can escape (red) and that are bounded by self-gravity (blue). We plot the tracer particle distribution according to its initial (left panel) and final (right panel) position. The initial profile demonstrates which part of the star is being ejected after deflagration. Compared with Figure 5, most of the innermost part of the ash is trapped in the star. Instead, most material within 200 km of its original position is trapped, while the particles between 200 and 500 km along the diagonal are partially ejected. The trapped matter in this region is consistent with the flame structure seen in Figure 5. We plot the final position of the ejected particles in the right panel at 10 s after the simulation. The mixing effects can no longer be seen. The ejected matter locates at the outermost part of the star, while the trapped matter falls back to form the remnant. The trapped matter is already settled down in the innermost 20,000 km. A careful examination at the density of the particles reveals some differences between the ejected ash and ejected fuel. The ejected ash has a lower tracer particle density compared to the ejected fuel. This is related to the thermal expansion of the ash when it arrives in the region filled with the cold fuel.

In Figure 7, we plot $[X_i/^{56}\mathrm{Fe}]$ for the characteristic model. Here

$$[X_i/^{56}\mathrm{Fe}] = \log[(X_i/^{56}\mathrm{Fe})/(X_i/^{56}\mathrm{Fe})_\odot] \quad (1)$$

is the mass fraction ratio to ^{56}Fe of the stable isotopes, relative to the solar ratio. Here the stable isotopes mean that all typical short-lifetime radioactive isotopes have decayed. After the

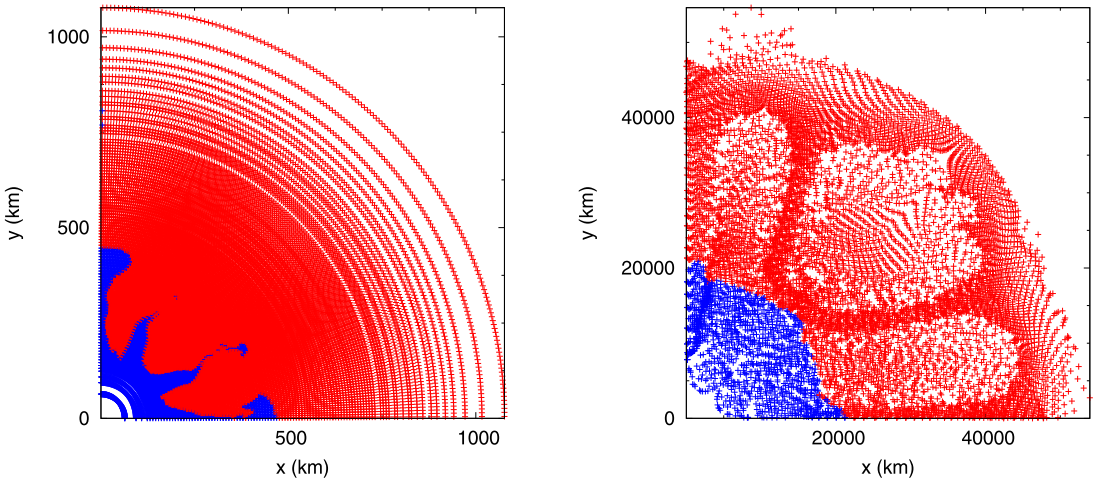

Figure 6. Tracer particle distribution for the particles that can escape (red) and are gravitationally bound (blue). The escape criterion is decided by the final energy of the tracer particles. The initial (left panel) and final (right panel) particle distributions are shown for comparison.

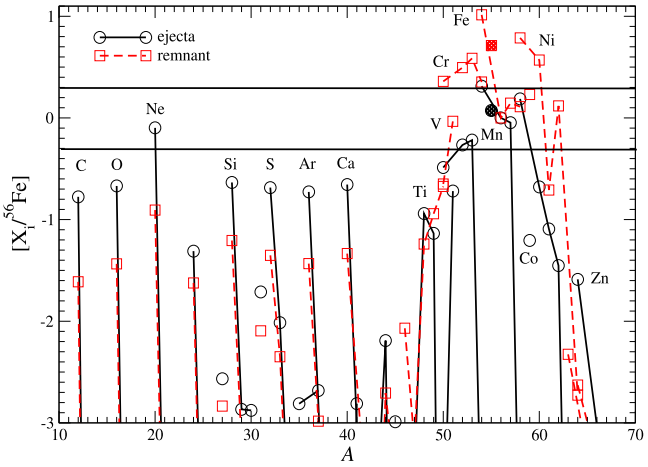

Figure 7. $[X_i/^{56}\mathrm{Fe}]$ against mass number for the characteristic model. The remnant and ejecta compositions are included.

postprocessing nucleosynthesis yield is obtained, we allow the yield product to decay for $\sim 10^6$ yr, such that most radioactive isotopes ^{56}Ni ($\sim$8 days), ^{57}Ni ($\sim$60 days), and ^{59}Ni (60,000 yr) have decayed. However, isotopes with a longer half-life, such as ^{27}Al and ^{60}Fe, may not have decayed completely. Despite that, these isotopes are not mostly produced in SNe Ia. Since the star is partially disrupted, we separate the ejecta and the remnant compositions for comparison. As shown in previous figures, the ejecta are obtained from the tracer particles, which have a positive total energy.

The ejecta mostly comes from matter in the surface, where O and Ne are abundant. It has very low masses of intermediate-mass elements (IMEs), such as Si, S, Ar, and Ca. The lower part of the iron-peak elements, i.e., Ti, V, and Cr, is also underproduced. On the contrary, the upper part of the iron-peak elements, i.e., Mn, Fe, and Ni, is well produced; Zn is underproduced.

The remnant has a similar pattern in O and Ne but is lower by 1 order of magnitude at 1%–10% of solar values. The abundances of IMEs in the deflagration ash are also low in the remnant, and they are still underproduced. The iron-peak elements have a more interesting pattern in the remnant. As discussed above, most tracer particles in the inner core failed to escape from the star during the momentum transfer process. The lower Y_e isotopes, including ^{54}Fe and ^{58}Ni, can be 10 and 8 times higher than the solar ratios. As a result, the lighter part of iron-peak elements, especially the neutron-rich ones including ^{51}V, ^{53,54}Cr, and ^{55}Mn, are higher than the solar ratios. In particular, $[^{55}\mathrm{Mn}/^{56}\mathrm{Fe}]$ and $[^{58}\mathrm{Ni}/^{56}\mathrm{Fe}]$ can reach $\sim$0.5 and 0.6, respectively. The final remnant WD has a very different composition from a standard C+O WD of similar mass ($\sim 0.3\ M_\odot$), where the contamination by IMEs and iron-peak elements is significant.

4. Model Summary

In this section, we examine the hydrodynamics and nucleosynthesis of our SN Iax models using PTD in C+O WDs and hybrid C+O+Ne WDs.

In Table 1, we tabulate the models computed in this work and their corresponding exploding energetics and global chemical properties. We name each model according to the model parameters. For example, the model 300-137-1-c3-06 means a C+O WD model with a central density 3.00×10^9 g cm^{-3}, CO-rich matter of mass 1.37 $M_\odot$, 1 $Z_\odot$, $c3$ flame, and C/O = 0.6 in mass fraction, i.e. $X(^{12}\mathrm{C}) = 0.366$, $X(^{16}\mathrm{O}) = 0.609$ and $X(^{22}\mathrm{Ne}) = 0.025$. For hybrid C+O+Ne WDs, the second entry is the mass of CO-rich matter before we mix the composition by hand. The last entry does not apply to hybrid C+O+Ne WDs.

5. Pure Turbulent Deflagration (PTD) in C+O White Dwarfs (WDs)

In this section, we study in detail the nucleosynthesis yields of C+O WDs, which explode as SNe Iax. For the C+O WDs with an initial central density $\rho_{\mathrm{c,\,ini}}$ and metallicity Z as the model parameters, we put in the initial centered or off-center flame. We follow the flame propagation and the expansion of the star until the star develops into homologous expansion. After that, we use the thermodynamical histories of the tracer particles to calculate the postprocess nucleosynthesis. In Tables 2–4, we tabulate the nucleosynthesis yield and radioactive isotopes in the ejecta.

Table 1
The Model Parameters of the Models Studied in This Work

Type	Model	ρ_c	Z	M	$M_{\rm CO}$	$M_{\rm ONe}$	Flame	R	$E_{\rm tot}$	$E_{\rm nuc}$	$M_{\rm ej}$	$M_{\rm rem}$	$M_{\rm Ni}$	Others
CO WD	050-130-1-c3-1	0.50	1	1.30	1.30	N/A	$c3$	3070	−1.61	2.36	0.00	1.30	0.00	C/O = 1
CO WD	100-133-1-c3-1	1.00	1	1.33	1.33	N/A	$c3$	2580	2.23	6.71	0.92	0.41	0.23	C/O = 1
CO WD	200-135-1-c3-1	2.00	1	1.35	1.35	N/A	$c3$	2170	3.69	8.52	1.18	0.17	0.24	C/O = 1
CO WD	300-137-1-c3-1	3.00	1	1.37	1.37	N/A	$c3$	1950	4.54	9.69	1.26	0.11	0.34	C/O = 1
CO WD	500-138-1-c3-1	5.00	1	1.38	1.38	N/A	$c3$	1710	5.13	10.5	1.29	0.09	0.32	C/O = 1
CO WD	550-138-1-c3-1	5.50	1	1.38	1.38	N/A	$c3$	1670	5.81	11.0	1.30	0.08	0.31	C/O = 1
CO WD	600-138-1-c3-1	6.00	1	1.38	1.38	N/A	$c3$	1620	6.03	11.2	1.31	0.07	0.30	C/O = 1
CO WD	750-139-1-c3-1	7.50	1	1.39	1.39	N/A	$c3$	1540	6.25	11.5	1.33	0.06	0.32	C/O = 1
CO WD	800-139-1-c3-1	8.00	1	1.39	1.39	N/A	$c3$	1500	7.51	12.7	1.34	0.05	0.31	C/O = 1
CO WD	900-140-1-c3-1	9.00	1	1.40	1.40	N/A	$c3$	1460	7.81	13.1	1.36	0.04	0.34	C/O = 1
CO WD	100-133-1-b1-1	1.00	1	1.33	1.33	N/A	$b1$	2580	2.99	7.47	1.03	0.30	0.23	C/O = 1
CO WD	300-137-1-b1-1	3.00	1	1.37	1.37	N/A	$b1$	1950	4.82	9.97	1.19	0.19	0.26	C/O = 1
CO WD	500-138-1-b1-1	5.00	1	1.38	1.38	N/A	$b1$	1710	6.50	11.9	1.20	0.18	0.30	C/O = 1
CO WD	550-138-1-b1-1	5.50	1	1.38	1.38	N/A	$b1$	1670	6.50	11.9	1.20	0.18	0.29	C/O = 1
CONe WD	100-043-1-c3	1.00	1	1.33	0.43	0.90	$c3$	2580	1.89	6.30	0.96	0.37	0.18	
CONe WD	200-045-1-c3	2.00	1	1.35	0.45	0.90	$c3$	2160	2.93	7.74	1.11	0.24	0.24	
CONe WD	300-047-1-c3	3.00	1	1.37	0.47	0.90	$c3$	1950	4.54	9.69	1.15	0.22	0.28	
CONe WD	500-048-1-c3	5.00	1	1.38	0.48	0.90	$c3$	1710	5.13	10.5	1.26	0.12	0.36	
CONe WD	550-048-1-c3	5.50	1	1.38	0.48	0.90	$c3$	1670	4.42	9.59	1.26	0.12	0.33	
CONe WD	750-049-1-c3	7.50	1	1.39	0.49	0.90	$c3$	1540	5.39	10.6	1.29	0.10	0.35	
CONe WD	900-050-1-c3	9.00	1	1.40	0.50	0.90	$c3$	1460	5.92	11.1	1.33	0.07	0.36	
CONe WD	100-043-1-b1	1.00	1	1.33	0.43	0.90	$b1$	2580	2.69	7.15	0.97	0.36	0.20	
CONe WD	200-045-1-b1	1.00	1	1.35	0.45	0.90	$b1$	2160	3.78	8.68	1.10	0.25	0.23	
CONe WD	300-047-1-b1	3.00	1	1.37	0.47	0.90	$b1$	1950	4.66	9.78	1.12	0.25	0.31	
CONe WD	500-048-1-b1	5.00	1	1.38	0.48	0.90	$b1$	1710	5.13	10.5	1.17	0.21	0.32	
CONe WD	550-048-1-b1	5.50	1	1.38	0.48	0.90	$b1$	1670	5.81	11.0	1.18	0.20	0.32	
CONe WD	750-049-1-b1	7.50	1	1.39	0.49	0.90	$b1$	1540	5.72	11.3	1.21	0.18	0.32	
CONe WD	900-050-1-b1	9.00	1	1.40	0.50	0.90	$b1$	1460	7.81	13.1	1.30	0.10	0.35	

Note. "Type" corresponds to the classification of the WD as a C+O or hybrid C+O+Ne WD. Here M, $M_{\rm CO}$, $M_{\rm ONe}$, $M_{\rm Ni}$, $M_{\rm ej}$, and $M_{\rm rem}$ are the mass of the initial WD, the C+O part, the O+Ne part, the total ^{56}Ni produced in the ejecta, the ejecta mass, and the remnant mass in units of $M_\odot$. Here R and $R_{\rm core}$ are the radius of the initial WD and the core (if applicable) in units of km, $E_{\rm tot}$ and $E_{\rm nuc}$ are the final total energy and the nuclear energy produced by the deflagration in units of 10^{50} erg, Z is the metallicity in units of $Z_\odot$, and ρ_c and $\rho_{\rm core}$ are the initial central density and core–envelope interface density (if applicable) in units of 10^9 g cm^{-3}. The notation "flame" corresponds to the initial geometry of the flame, including $c3$ (three-finger) and $b1$ (one-bubble) structure. "Others" includes settings specific to that corresponding type of WD.

5.1. Ejecta of C+O WD

5.1.1. Dependence on Central Density of WD

In Figure 8, we plot the abundance ratios $[X/^{56}\mathrm{Fe}]$ in the ejecta of models 100-133-1-c3-1 ($\rho_c = 10^9$ g cm^{-3}), 300-137-1-c3-1 ($\rho_c = 3 \times 10^9$ g cm^{-3}), 500-137-1-c3-1 ($\rho_c = 5 \times 10^9$ g cm^{-3}), and 800-137-1-c3-1 ($\rho_c = 8 \times 10^9$ g cm^{-3}). These are the models based on C+O WDs with different ρ_c. In the top panel, we plot the abundance patterns for models 100-133-1-c3-1 and 500-133-1-c3-1, while in the bottom panel, we plot the other two. More IMEs appear in the ejecta of higher ρ_c, except for the very high $\rho_c = 8 \times 10^9$ g cm^{-3}. At low density ($(1–5) \times 10^9$ g cm^{-3}), the iron-peak elements are comparable to the solar ratios with larger $[X/\mathrm{Fe}]$ for higher ρ_c. Isotope ratios, including ^{50,52,53}Cr, ^{54}Fe, ^{55}Mn, and ^{58}Ni, are larger for higher ρ_c. At high ρ_c, the increase in ^{54}Fe, ^{55}Mn, and ^{58}Ni levels off. Instead, neutron-rich isotopes, including ^{51}V, ^{54}Cr, ^{60}Fe, and ^{62}Ni, become severely overproduced relative to the solar ratio.

5.1.2. Dependence on Initial Flame Structure

We examine the effects of initial flame structure on the nucleosynthesis yield for the C+O WD models. In Figure 9, we plot $[X/^{56}\mathrm{Fe}]$ in the ejecta for models 300-137-1-c3-1 ($c3$ flame) and 300-137-1-b1-1 ($b1$ flame). The two WD models share the same configuration but with different initial flame geometry.

The differences between the two models are small. The IMEs show systematic downward shifts when the initial flame moves from center to off-center. This suggests that the mass of ^{56}Fe as the denominator changes instead of the change in individual isotope yields. Similar changes can be observed for the iron-peak elements too. On the contrary, the off-center burning facilitates the production of iron-peak elements. It is because the iron-peak elements produced in the off-center initial flame can be more readily ejected than those produced at the center.

However, we remark that the effects in the three-dimensional model can be larger, as shown in Röpke et al. (2006a), Seitenzahl et al. (2013), and Fink et al. (2014). Three-dimensional simulations can accommodate a more complex flame structure and hence more diversified distributions in the ejecta abundance.

5.1.3. Dependence on C/O Ratio

We examine the effects of the initial C/O ratio on the nucleosynthesis yields of the C+O WD models. The

Table 2
Mass of Major Isotopes in the Ejecta after All Short-lived Radioactive Isotopes Have Decayed

Isotopes	100-133-1-c3-1	200-135-1-c3-1	300-137-1-c3-1	500-138-1-c3-1	550-138-1-c3-1	750-139-1-c3-1	900-140-1-c3-1
^{12}C	2.96×10^{-1}	3.81×10^{-1}	3.21×10^{-1}	3.14×10^{-1}	3.14×10^{-1}	2.43×10^{-1}	1.82×10^{-1}
^{13}C	6.56×10^{-12}	4.44×10^{-11}	6.50×10^{-11}	6.55×10^{-11}	5.31×10^{-11}	1.42×10^{-10}	2.9×10^{-10}
^{14}N	9.12×10^{-10}	3.85×10^{-9}	5.85×10^{-9}	5.37×10^{-9}	4.72×10^{-9}	1.23×10^{-8}	1.87×10^{-8}
^{15}N	2.77×10^{-10}	1.44×10^{-9}	1.44×10^{-9}	1.29×10^{-9}	1.43×10^{-9}	3.17×10^{-9}	4.53×10^{-9}
^{16}O	3.1×10^{-1}	4.8×10^{-1}	3.54×10^{-1}	3.44×10^{-1}	3.40×10^{-1}	3.17×10^{-1}	2.82×10^{-1}
^{17}O	2.96×10^{-10}	1.33×10^{-9}	2.9×10^{-9}	1.93×10^{-9}	1.70×10^{-9}	4.41×10^{-9}	6.78×10^{-9}
^{18}O	9.15×10^{-12}	3.86×10^{-11}	6.27×10^{-11}	5.59×10^{-11}	5.2×10^{-11}	1.29×10^{-10}	1.99×10^{-10}
^{19}F	3.57×10^{-12}	1.52×10^{-11}	1.81×10^{-11}	1.75×10^{-11}	1.65×10^{-11}	4.23×10^{-11}	6.14×10^{-11}
^{20}Ne	7.40×10^{-4}	3.10×10^{-3}	3.23×10^{-3}	3.17×10^{-3}	3.17×10^{-3}	8.1×10^{-3}	1.11×10^{-2}
^{21}Ne	2.46×10^{-8}	1.3×10^{-7}	1.8×10^{-7}	1.12×10^{-7}	1.3×10^{-7}	2.80×10^{-7}	3.88×10^{-7}
^{22}Ne	1.20×10^{-2}	1.55×10^{-2}	1.31×10^{-2}	1.28×10^{-2}	1.28×10^{-2}	9.90×10^{-3}	7.43×10^{-3}
^{23}Na	2.20×10^{-6}	9.76×10^{-6}	1.5×10^{-5}	1.5×10^{-5}	1.2×10^{-5}	2.49×10^{-5}	3.62×10^{-5}
^{24}Mg	7.48×10^{-4}	3.58×10^{-3}	3.99×10^{-3}	3.75×10^{-3}	3.44×10^{-3}	9.1×10^{-3}	1.18×10^{-2}
^{25}Mg	5.9×10^{-6}	1.98×10^{-5}	2.20×10^{-5}	2.13×10^{-5}	2.6×10^{-5}	5.39×10^{-5}	7.45×10^{-5}
^{26}Mg	7.24×10^{-6}	3.14×10^{-5}	3.35×10^{-5}	3.28×10^{-5}	3.20×10^{-5}	8.3×10^{-5}	1.14×10^{-4}
^{26}Al	2.39×10^{-29}	3.6×10^{-29}	3.27×10^{-29}	9.62×10^{-10}	9.33×10^{-10}	2.54×10^{-9}	3.53×10^{-29}
^{27}Al	6.4×10^{-5}	2.67×10^{-4}	3.1×10^{-4}	2.78×10^{-4}	2.59×10^{-4}	7.23×10^{-4}	9.40×10^{-4}
^{28}Si	1.21×10^{-2}	3.64×10^{-2}	4.0×10^{-2}	4.36×10^{-2}	3.61×10^{-2}	5.5×10^{-2}	6.3×10^{-2}
^{29}Si	6.71×10^{-5}	3.9×10^{-4}	3.51×10^{-4}	3.36×10^{-4}	2.97×10^{-4}	8.21×10^{-4}	1.10×10^{-3}
^{30}Si	9.78×10^{-5}	4.89×10^{-4}	5.78×10^{-4}	5.34×10^{-4}	4.62×10^{-4}	1.36×10^{-3}	1.78×10^{-3}
^{31}P	2.52×10^{-5}	1.6×10^{-4}	1.27×10^{-4}	1.17×10^{-4}	1.0×10^{-4}	2.98×10^{-4}	3.92×10^{-4}
^{32}S	6.28×10^{-3}	1.61×10^{-2}	1.75×10^{-2}	1.92×10^{-2}	1.58×10^{-2}	1.97×10^{-2}	2.25×10^{-2}
^{33}S	1.99×10^{-5}	7.75×10^{-5}	9.38×10^{-5}	8.88×10^{-5}	7.29×10^{-5}	2.23×10^{-4}	2.91×10^{-4}
^{34}S	1.6×10^{-4}	5.7×10^{-4}	6.13×10^{-4}	6.2×10^{-4}	4.76×10^{-4}	1.8×10^{-3}	1.47×10^{-3}
^{36}S	1.2×10^{-8}	4.88×10^{-8}	5.80×10^{-8}	5.46×10^{-8}	4.62×10^{-8}	1.52×10^{-7}	1.97×10^{-7}
^{35}Cl	1.11×10^{-5}	3.30×10^{-5}	3.82×10^{-5}	3.62×10^{-5}	3.24×10^{-5}	7.73×10^{-5}	1.6×10^{-4}
^{37}Cl	1.84×10^{-6}	5.6×10^{-6}	5.83×10^{-6}	6.19×10^{-6}	4.75×10^{-6}	8.54×10^{-6}	1.10×10^{-5}
^{36}Ar	1.15×10^{-3}	2.60×10^{-3}	2.83×10^{-3}	3.6×10^{-3}	2.53×10^{-3}	2.69×10^{-3}	2.89×10^{-3}
^{38}Ar	6.68×10^{-5}	2.33×10^{-4}	2.71×10^{-4}	2.83×10^{-4}	2.21×10^{-4}	2.87×10^{-4}	3.46×10^{-4}
^{40}Ar	1.71×10^{-10}	6.25×10^{-10}	7.50×10^{-10}	6.68×10^{-10}	5.94×10^{-10}	2.42×10^{-9}	3.11×10^{-9}
^{39}K	6.49×10^{-6}	1.64×10^{-5}	1.82×10^{-5}	1.98×10^{-5}	1.49×10^{-5}	1.96×10^{-5}	2.61×10^{-5}
^{40}K	3.89×10^{-9}	9.94×10^{-9}	1.19×10^{-8}	1.3×10^{-8}	9.65×10^{-9}	3.31×10^{-8}	4.39×10^{-8}
^{41}K	4.85×10^{-7}	1.9×10^{-6}	1.14×10^{-6}	1.27×10^{-6}	9.28×10^{-7}	1.17×10^{-6}	1.47×10^{-6}
^{40}Ca	1.4×10^{-3}	2.12×10^{-3}	2.34×10^{-3}	2.47×10^{-3}	2.5×10^{-3}	1.98×10^{-3}	1.97×10^{-3}
^{42}Ca	2.28×10^{-6}	6.57×10^{-6}	7.47×10^{-6}	7.98×10^{-6}	6.8×10^{-6}	8.44×10^{-6}	1.3×10^{-5}
^{43}Ca	7.46×10^{-9}	1.55×10^{-8}	2.24×10^{-8}	1.92×10^{-8}	1.62×10^{-8}	5.71×10^{-8}	7.92×10^{-8}
^{44}Ca	8.41×10^{-7}	1.40×10^{-6}	1.87×10^{-6}	1.84×10^{-6}	1.56×10^{-6}	1.84×10^{-6}	2.3×10^{-6}
^{46}Ca	2.80×10^{-12}	9.47×10^{-12}	1.29×10^{-11}	1.31×10^{-11}	2.82×10^{-10}	6.17×10^{-9}	4.36×10^{-8}
^{48}Ca	1.68×10^{-17}	5.34×10^{-17}	6.59×10^{-17}	2.66×10^{-14}	2.3×10^{-11}	3.11×10^{-9}	1.78×10^{-6}
^{45}Sc	1.84×10^{-8}	3.64×10^{-8}	4.41×10^{-8}	4.68×10^{-8}	3.63×10^{-8}	7.75×10^{-8}	9.94×10^{-8}
^{46}Ti	1.6×10^{-6}	2.86×10^{-6}	3.20×10^{-6}	3.64×10^{-6}	2.65×10^{-6}	3.27×10^{-6}	3.98×10^{-6}
^{47}Ti	4.20×10^{-8}	7.71×10^{-8}	1.6×10^{-7}	1.10×10^{-7}	9.56×10^{-8}	1.96×10^{-7}	2.77×10^{-7}
^{48}Ti	2.22×10^{-5}	3.68×10^{-5}	4.80×10^{-5}	4.75×10^{-5}	4.42×10^{-5}	4.97×10^{-5}	5.6×10^{-5}
^{49}Ti	1.96×10^{-6}	3.40×10^{-6}	4.77×10^{-6}	5.27×10^{-6}	5.34×10^{-6}	6.74×10^{-6}	1.29×10^{-5}
^{50}Ti	2.47×10^{-11}	6.76×10^{-11}	2.84×10^{-10}	8.4×10^{-7}	5.20×10^{-5}	6.77×10^{-4}	3.68×10^{-3}
^{50}V	1.74×10^{-10}	4.0×10^{-10}	1.44×10^{-9}	6.51×10^{-9}	2.43×10^{-8}	7.21×10^{-8}	1.3×10^{-7}
^{51}V	9.23×10^{-6}	1.45×10^{-5}	2.73×10^{-5}	3.60×10^{-5}	6.88×10^{-5}	2.36×10^{-4}	5.16×10^{-4}

Note. The isotope masses are in units of solar mass.

uncertainty in the C/O ratio mainly stems from the uncertainties in the ^{12}C(α, γ)^{16}O rate and the convective overshooting during He burning in the progenitor.

In Figure 10, we plot [X/^{56}Fe] in the ejecta for models 300-137-1-c3-06 (C/O = 0.6) and 300-137-1-c3-03 (C/O = 0.3). The two WD models share the same configuration but with different a C/O ratio. The uncertainties of the C/O ratio originate from the model parameters from stellar evolution including the less constrained ^{12}C (α, γ^{16})O rates and the uncertainties of the progenitor main-sequence star mass and metallicity during the mass accretion and simmering phases.

The effects of the C/O ratio are much smaller than the previous two parameters. We find almost no change in iron-peak elements, and there are small enhancements in the IMEs when the C/O ratio is low. This is because a slower flame for the lower C/O ratio produces lower energy; thus, the amount of matter experiencing incomplete burning increases. However, the effects are limited by the amount of ash, which is determined by WD expansion.

5.1.4. Dependence on Turbulent Flame Speed

We examine the effects of turbulent flame speed on the nucleosynthesis yield of the C+O WD models. In Figure 11,

Table 3
(cont'd) Mass of Major Isotopes in the Ejecta after All Short-lived Radioactive Isotopes Have Decayed

Isotopes	100-133-1-c3-1	200-135-1-c3-1	300-137-1-c3-1	500-138-1-c3-1	550-138-1-c3-1	750-139-1-c3-1	900-140-1-c3-1
^{50}Cr	3.53×10^{-5}	6.40×10^{-5}	1.46×10^{-4}	2.5×10^{-4}	2.19×10^{-4}	2.49×10^{-4}	2.74×10^{-4}
^{52}Cr	7.60×10^{-4}	1.13×10^{-3}	2.1×10^{-3}	3.25×10^{-3}	6.4×10^{-3}	1.25×10^{-2}	1.63×10^{-2}
^{53}Cr	1.36×10^{-4}	1.94×10^{-4}	4.59×10^{-4}	6.56×10^{-4}	8.40×10^{-4}	1.36×10^{-3}	1.93×10^{-3}
^{54}Cr	1.14×10^{-8}	3.74×10^{-8}	1.47×10^{-6}	2.22×10^{-5}	6.20×10^{-4}	5.33×10^{-3}	1.99×10^{-2}
^{55}Mn	2.56×10^{-3}	3.29×10^{-3}	7.18×10^{-3}	9.3×10^{-3}	1.1×10^{-2}	1.27×10^{-2}	1.53×10^{-2}
^{54}Fe	2.5×10^{-2}	2.89×10^{-2}	7.40×10^{-2}	9.76×10^{-2}	1.5×10^{-1}	1.16×10^{-1}	1.23×10^{-1}
^{56}Fe	2.32×10^{-1}	2.42×10^{-1}	3.49×10^{-1}	3.55×10^{-1}	3.62×10^{-1}	4.8×10^{-1}	4.46×10^{-1}
^{57}Fe	7.41×10^{-3}	7.65×10^{-3}	1.20×10^{-2}	1.22×10^{-2}	1.24×10^{-2}	1.38×10^{-2}	1.57×10^{-2}
^{58}Fe	3.53×10^{-8}	9.64×10^{-8}	2.73×10^{-6}	1.13×10^{-4}	2.34×10^{-3}	1.42×10^{-2}	3.86×10^{-2}
^{60}Fe	1.60×10^{-20}	5.82×10^{-20}	4.49×10^{-17}	4.39×10^{-11}	4.54×10^{-9}	1.14×10^{-7}	1.53×10^{-5}
^{59}Co	1.26×10^{-4}	1.19×10^{-4}	4.5×10^{-4}	5.85×10^{-4}	7.6×10^{-4}	1.1×10^{-3}	1.26×10^{-3}
^{58}Ni	2.13×10^{-2}	2.36×10^{-2}	4.69×10^{-2}	5.47×10^{-2}	5.69×10^{-2}	6.11×10^{-2}	6.44×10^{-2}
^{60}Ni	7.6×10^{-4}	6.97×10^{-4}	3.25×10^{-3}	5.45×10^{-3}	6.76×10^{-3}	8.81×10^{-3}	1.5×10^{-2}
^{61}Ni	2.45×10^{-5}	2.11×10^{-5}	3.93×10^{-5}	3.31×10^{-5}	4.75×10^{-5}	8.95×10^{-5}	1.72×10^{-4}
^{62}Ni	2.11×10^{-4}	1.74×10^{-4}	2.79×10^{-4}	2.94×10^{-4}	1.10×10^{-3}	4.26×10^{-3}	8.59×10^{-3}
^{64}Ni	8.88×10^{-15}	1.84×10^{-12}	3.4×10^{-12}	3.60×10^{-8}	2.36×10^{-6}	4.16×10^{-5}	1.34×10^{-3}
^{63}Cu	1.47×10^{-7}	1.8×10^{-7}	2.31×10^{-7}	2.53×10^{-7}	7.61×10^{-7}	3.76×10^{-6}	1.95×10^{-5}
^{65}Cu	5.51×10^{-8}	4.91×10^{-8}	1.40×10^{-7}	7.48×10^{-8}	1.17×10^{-7}	4.96×10^{-7}	3.0×10^{-6}
^{64}Zn	4.29×10^{-7}	3.68×10^{-7}	9.7×10^{-7}	6.43×10^{-7}	5.93×10^{-7}	8.88×10^{-7}	1.25×10^{-6}
^{66}Zn	9.51×10^{-7}	8.1×10^{-7}	1.72×10^{-6}	1.12×10^{-6}	1.1×10^{-6}	1.67×10^{-6}	2.50×10^{-5}
^{67}Zn	5.57×10^{-10}	4.61×10^{-10}	1.37×10^{-9}	6.64×10^{-10}	1.88×10^{-9}	3.4×10^{-9}	1.15×10^{-6}
^{68}Zn	2.14×10^{-10}	4.97×10^{-10}	5.35×10^{-10}	3.13×10^{-10}	6.52×10^{-9}	3.70×10^{-8}	4.43×10^{-7}
^{70}Zn	1.77×10^{-22}	1.51×10^{-12}	5.64×10^{-22}	1.24×10^{-15}	1.41×10^{-10}	1.73×10^{-11}	7.49×10^{-8}

Note. The isotope masses are in units of solar mass.

Table 4
Masses of the Radioactive Isotopes in the Ejecta after the Explosion

Isotopes	100-133-1-c3-1	200-135-1-c3-1	300-137-1-c3-1	500-138-1-c3-1	550-138-1-c3-1	750-139-1-c3-1	900-140-1-c3-1
^{22}Na	2.29×10^{-9}	9.80×10^{-9}	1.6×10^{-8}	1.0×10^{-8}	9.79×10^{-9}	2.62×10^{-8}	3.66×10^{-8}
^{26}Al	1.11×10^{-6}	4.61×10^{-6}	4.82×10^{-6}	5.12×10^{-6}	4.85×10^{-6}	1.22×10^{-5}	1.69×10^{-5}
^{39}Ar	7.40×10^{-10}	2.13×10^{-9}	2.2×10^{-9}	1.94×10^{-9}	2.1×10^{-9}	6.51×10^{-9}	9.2×10^{-9}
^{40}K	3.91×10^{-9}	1.11×10^{-8}	1.4×10^{-8}	9.70×10^{-9}	1.5×10^{-8}	3.33×10^{-8}	4.42×10^{-8}
^{41}Ca	4.29×10^{-7}	1.0×10^{-6}	1.23×10^{-6}	8.93×10^{-7}	1.11×10^{-6}	1.15×10^{-6}	1.46×10^{-6}
^{44}Ti	8.12×10^{-7}	1.64×10^{-6}	1.74×10^{-6}	1.51×10^{-6}	1.52×10^{-6}	1.68×10^{-6}	1.81×10^{-6}
^{48}V	3.94×10^{-9}	8.54×10^{-9}	1.5×10^{-8}	8.45×10^{-9}	1.2×10^{-8}	1.24×10^{-8}	1.63×10^{-8}
^{49}V	8.9×10^{-9}	4.31×10^{-8}	9.30×10^{-8}	1.20×10^{-7}	1.57×10^{-7}	2.21×10^{-7}	2.80×10^{-7}
^{53}Mn	3.43×10^{-6}	1.61×10^{-4}	3.67×10^{-4}	4.60×10^{-4}	5.51×10^{-4}	5.96×10^{-4}	6.99×10^{-4}
^{60}Fe	2.48×10^{-19}	6.76×10^{-16}	6.14×10^{-10}	6.36×10^{-8}	1.52×10^{-7}	1.59×10^{-6}	2.25×10^{-4}
^{56}Co	1.96×10^{-5}	7.1×10^{-5}	1.0×10^{-4}	1.9×10^{-4}	1.11×10^{-4}	1.23×10^{-4}	1.30×10^{-4}
^{57}Co	2.39×10^{-5}	6.48×10^{-4}	1.26×10^{-3}	1.45×10^{-3}	1.57×10^{-3}	1.71×10^{-3}	1.93×10^{-3}
^{60}Co	9.31×10^{-14}	5.13×10^{-11}	1.94×10^{-8}	3.3×10^{-7}	6.8×10^{-7}	1.58×10^{-6}	4.3×10^{-6}
^{56}Ni	2.32×10^{-1}	3.9×10^{-1}	3.21×10^{-1}	3.8×10^{-1}	3.1×10^{-1}	3.18×10^{-1}	3.39×10^{-1}
^{57}Ni	7.39×10^{-3}	1.4×10^{-2}	1.9×10^{-2}	1.6×10^{-2}	1.5×10^{-2}	1.11×10^{-2}	1.21×10^{-2}
^{59}Ni	1.64×10^{-5}	2.36×10^{-4}	4.36×10^{-4}	4.89×10^{-4}	5.13×10^{-4}	5.63×10^{-4}	6.31×10^{-4}
^{63}Ni	1.96×10^{-15}	3.20×10^{-12}	1.41×10^{-8}	3.73×10^{-7}	8.4×10^{-7}	2.84×10^{-6}	1.70×10^{-5}

Note. The isotope masses are in units of solar mass.

we plot the final abundance pattern of the ejecta for models 300-137-1-c3-1-f05 and 300-137-1-c3-1-f025. The two WD models share the same configuration but with different asymptotic turbulent flame speeds (at 50% and 25% of the standard prescription). That means that we alter C_A in the turbulent flame speed formula,

$$v_{\rm flame} = v_{\rm lam}(\rho)\sqrt{1 + C_A(v'/v_{\rm lam})^2}\,, \quad (2)$$

where $v_{\rm lam}(\rho)$ and v' are the laminar flame propagation speed and the velocity fluctuations due to turbulent motion. We can see that at $v' \to 0$, $v_{\rm flame} = v_{\rm lam}(\rho)$. This means that the flame propagates like a laminar wave when the flow is not turbulent. Otherwise, when $v' \gg v_{\rm lam}$, $v_{\rm flame} \to \sqrt{C_A}\,v'$. This means that the flame burns with a speed following the turbulent motion.

We remark that the connection between the turbulent velocity fluctuations v' and the corresponding flame velocity is not yet well constrained because the corresponding WD

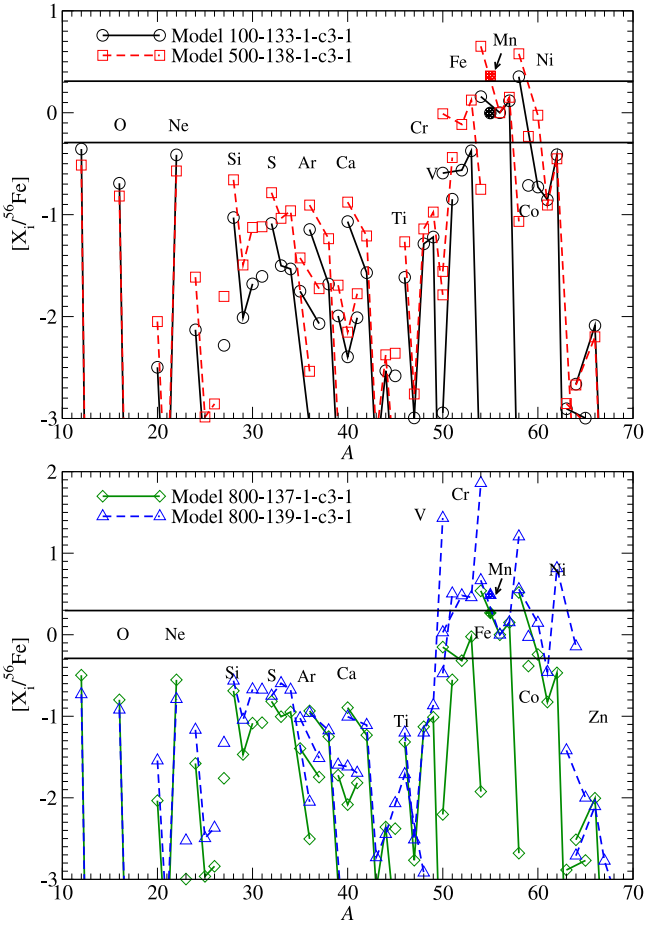

Figure 8. $[X_i/^{56}\mathrm{Fe}]$ against mass number for the ejecta of C+O WD models for models 100-133-1-c3-1 ($\rho_c = 1 \times 10^9$ g cm^{-3}) and 500-138-1-c3-1 ($\rho_c = 5 \times 10^9$ g cm^{-3}) in the top panel and 300-137-1-c3-1 ($\rho_c = 3 \times 10^9$ g cm^{-3}) and 800-138-1-c3-1 ($\rho_c = 8 \times 10^9$ g cm^{-3}) in the bottom panel. All models assume no hybrid O+Ne+Mg-rich matter, $X(^{22}\mathrm{Ne}) = 0.025$, $c3$ initial flame, and C/O ratio = 1.

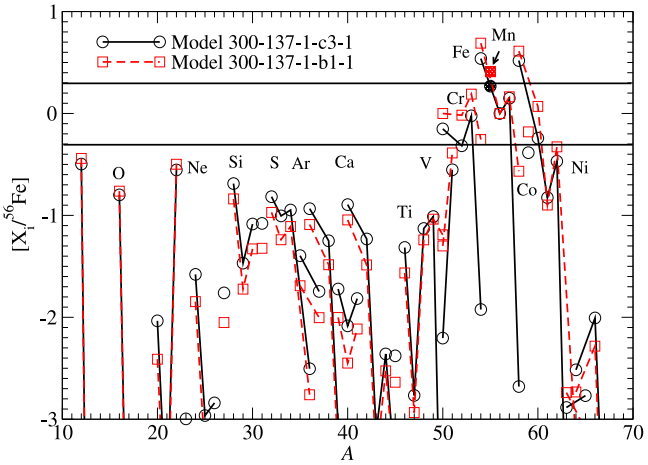

Figure 9. Scaled mass fraction $[X_i/^{56}\mathrm{Fe}]$ against mass number for the ejecta of C+O WD models for models 300-137-1-c3-1 ($c3$ flame) and 300-137-1-b1-1 ($b1$ flame). All models assume $\rho_c = 3 \times 10^9$ g cm^{-3}, no hybrid O+Ne+Mg-rich matter, $X(^{22}\mathrm{Ne}) = 0.025$, and C/O ratio = 1.

condition and environment cannot be reproduced in any laboratory. It is unclear how the flame speed scales with v' in the turbulent regime, where, in a WD, the Reynolds number

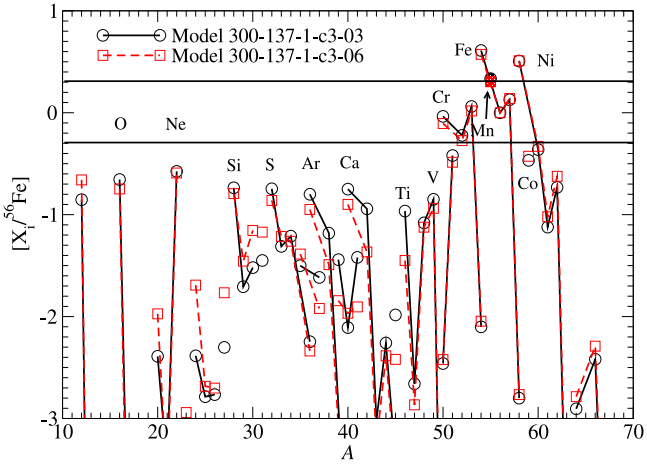

Figure 10. Scaled mass fraction $[X_i/^{56}\mathrm{Fe}]$ against mass number for the ejecta of C+O WD models for models 300-137-1-c3-06 (C/O = 0.6) and 300-137-1-c3-03 (C/O = 0.3). All models assume $\rho_c = 3 \times 10^9$ g cm^{-3}, no hybrid O+Ne+Mg-rich matter, $X(^{22}\mathrm{Ne}) = 0.025$, and $c3$ initial flame.

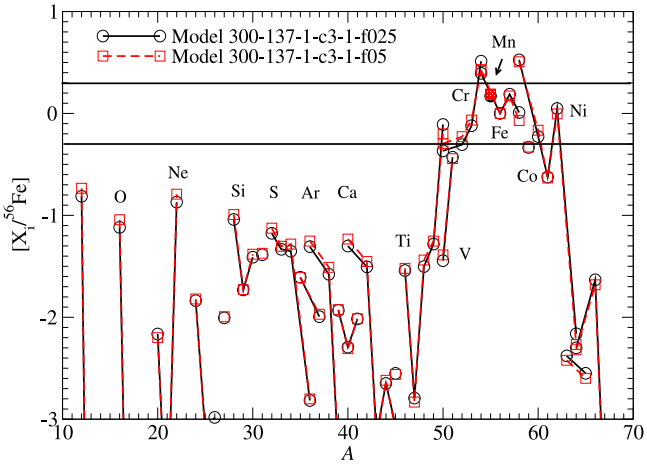

Figure 11. $[X_i/^{56}\mathrm{Fe}]$ against mass number for the ejecta for models 300-137-1-c3-1-f05 ($v_{\mathrm{flame}} = 0.5\ v_{\mathrm{flame},0}$) and 300-137-1-c3-1-f025 ($v_{\mathrm{flame}} = 0.25\ v_{\mathrm{flame},0}$). All models assume $\rho_c = 3 \times 10^9$ g cm^{-3}, no hybrid O+Ne+Mg-rich layer, $X(^{22}\mathrm{Ne}) = 0.025$, $c3$ initial flame, and C/O ratio = 1.

can be as high as 10^{14}. A formula based on theoretical arguments can be found in, e.g., Hicks (2015).

In contrast to our previous works, the flame velocity has almost no effect on the chemical yields of our models. There are very minor differences in IMEs.

5.2. Remnant of PTD in C+O WD

5.2.1. Dependence on Central Density

In Figure 12, we study the effects of initial ρ_c of the WD on the nucleosynthesis yields in the bounded remnant WDs. Similar to the characteristic model, the bounded remnant is defined by the tracer particles, which have a negative total energy at the end of the simulations (10 s after the flame starts). The effects of ρ_c are consistent with our earlier work (Leung & Nomoto 2018).

In the top panel, we plot models 100-000-1-c3-1 and 500-000-1-c3-1 of the remnant part, and in the bottom panel, we plot the other two models. Similar to the ejecta, with increasing ρ_c, masses of IMEs decrease. At a very high ρ_c, the remnant does not contain any C+O+Ne-rich matter or IMEs. This is

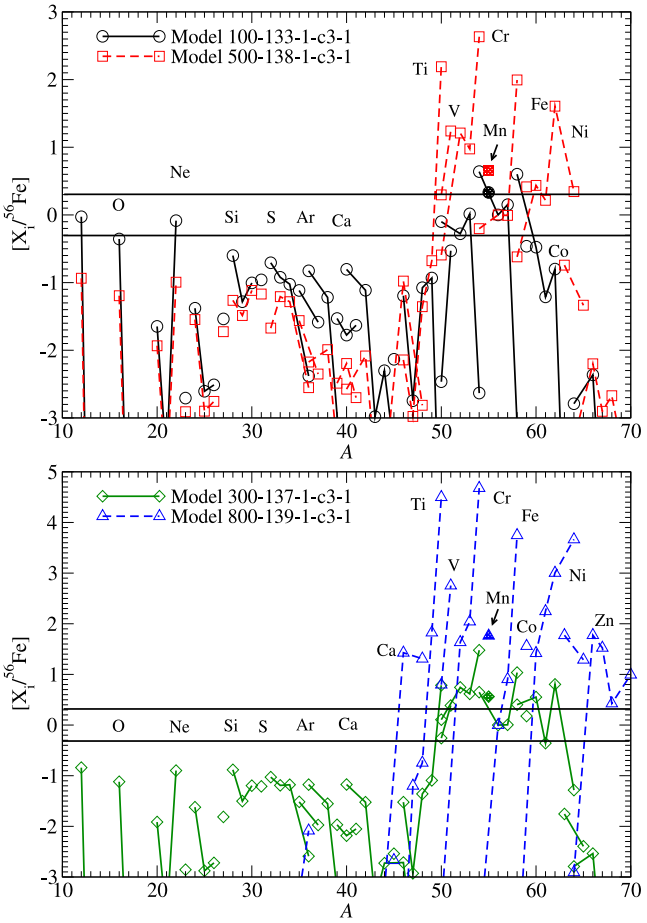

Figure 12. $[X_i/^{56}\mathrm{Fe}]$ against mass number for remnants of C+O WD models for models 100-130-1-c3-1 ($\rho_c = 1 \times 10^9$ g cm^{-3}) and 500-138-1-c3-1 ($\rho_c = 5 \times 10^9$ g cm^{-3}) in the top panel and 300-137-1-c3-1 ($\rho_c = 3 \times 10^9$ g cm^{-3}) and 800-139-1-c3-1 ($\rho_c = 8 \times 10^9$ g cm^{-3}) in the bottom panel. All models assume no hybrid O+Ne+Mg-rich matter, $X(^{22}\mathrm{Ne}) = 0.025$, $c3$ initial flame, and C/O ratio = 1.

because that matter, which is synthesized at an outer region with a lower density (10^8 g cm^{-3} or below), is also ejected without fallback by the stronger deflagration. In all models, IMEs are always underproduced. The drop of IMEs with an increasing progenitor mass is because more matter can be burned at a lower density before the flame quenches.

The iron-peak elements show more interesting features. Isotopes with a high Y_e gradually decrease in their abundance when ρ_c increases. Neutron-rich isotopes are robustly overproduced in the remnant. At a central density 3×10^9 g cm^{-3}, isotopes like ^{54}Cr and ^{58}Fe are overproduced, especially for models 500-138-1-c3-1 and 800-139-1-c3-1. At a higher ρ_c, iron-peak elements from Ca to Zn are found in the remnant. Their abundances can exceed the solar values by a factor of 10^{2-5} in model 800-139-1-c3-1.

We remark that in interpreting the remnant composition, it is also useful to examine the element abundances instead of the isotope abundances because the spectra from WD remnants do not distinguish isotopes. We also show the element distribution in Section 7.

5.2.2. Dependence on Initial Flame Structure

In Figure 13, we study the effects of the initial flame on the remnant nucleosynthesis pattern. We plot the abundance

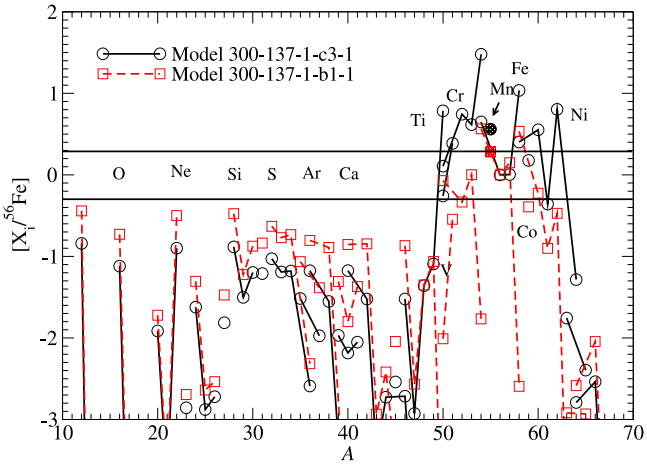

Figure 13. $[X_i/^{56}\mathrm{Fe}]$ against mass number for the bounded remnant of C+O WD models for models 300-137-1-c3-1 ($c3$ flame) and 300-137-1-b1-1 ($b1$ flame). All models assume $\rho_c = 3 \times 10^9$ g cm^{-3}, no hybrid O+Ne+Mg-rich matter, $X(^{22}\mathrm{Ne}) = 0.025$, and C/O ratio = 1.

pattern of models 300-137-1-c3-1 and 300-137-1-b1-1. They differ only by the position of the initial flame (center versus off-center). Consistent with the ejecta composition, the remnant consists of high abundances of IMEs when the flame is off-center. When the initial flame is farther from the center, the overproduction of some neutron-rich isotopes is less severe. This can be seen as a systematic drop in isotopes like $^{52-54}$Cr, ^{55}Mn, ^{58}Fe, and $^{60-64}$Ni. Higher Y_e isotopes of Fe and Ni remain similar. These features are generally consistent with the picture that the off-center flame can push matter more easily outward, as the momentum transport does not necessarily start in the center.

5.2.3. Dependence on C/O Ratio

In Figure 14, we plot the abundance pattern for the remnants of models 300-137-1-c3-06 and 300-137-1-c3-03. The two models differ by the C/O ratio, which changes not only the initial chemical composition but also the energy production by deflagration and the laminar flame speed. The differences between the two models are slightly stronger than the ejecta. Enhanced isotopes of IMEs such as ^{38}Ar and ^{42}Ca can be observed. The iron-peak elements are shifted upward systematically when the C/O ratio decreases, again suggesting the changes of ^{56}Fe.

5.2.4. Dependence on Turbulent Flame Speed

In Figure 15, we compare the effects of asymptotic turbulent flame speed on the remnant composition for models 300-137-1-c3-1-f025 and 300-137-1-c3-1-f05. Similar to the ejecta, the difference of flame speed we chose does not affect the abundance pattern at an observable level. A systematic decrease for most isotopes can be observed when v_{flame} increases, suggesting that the flame produces more ^{56}Fe as a result. When a slower flame model is used, a systematic enhancement of C+O-rich matter and IMEs can be found in the remnant. The abundances of neutron-rich iron-peak elements increase when the flame speed increases too. Meanwhile, there is no significant enhancement for iron-peak elements with a higher Y_e.

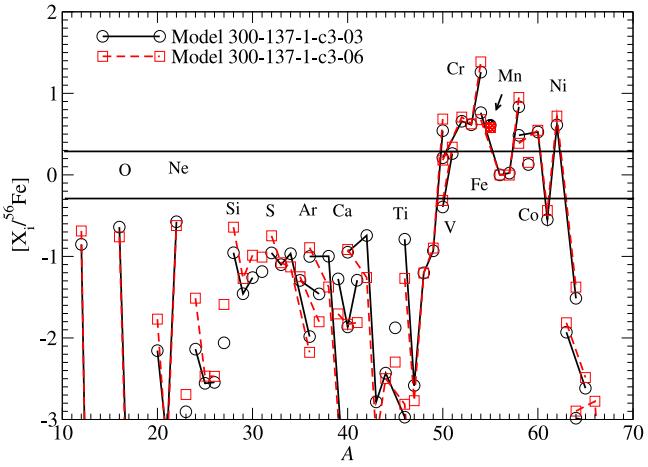

Figure 14. $[X_i/^{56}\mathrm{Fe}]$ against mass number for the bounded remnant of C+O WD models for models 300-137-1-c3-06 (C/O = 0.6) and 300-137-1-c3-03 (C/O = 0.3). All models assume $\rho_c = 3 \times 10^9$ g cm^{-3}, no hybrid O+Ne +Mg-rich matter, $X(^{22}\mathrm{Ne}) = 0.025$, and $c3$ initial flame.

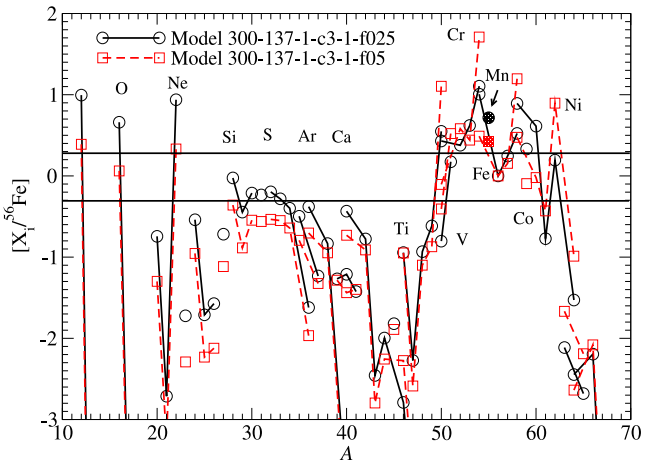

Figure 15. $[X_i/^{56}\mathrm{Fe}]$ against mass number for the bounded remnant of C+O WD models for models 300-137-1-c3-1-f025 ($v_{\mathrm{flame}} = 0.25\, v_{\mathrm{flame},0}$) and 300-137-1-c3-1-f05 ($v_{\mathrm{flame}} = 0.5\, v_{\mathrm{flame},0}$). All models assume $\rho_c = 3 \times 10^9$ g cm^{-3}, no hybrid O+Ne+Mg-rich matter, $X(^{22}\mathrm{Ne}) = 0.025$, $c3$ initial flame, and C/O ratio = 1.

6. Hybrid C+O+Ne WD

In this section, we study how the model parameters affect the explosive nucleosynthesis of the hybrid C+O+Ne WD. In Tables 5–7, we tabulate the nucleosynthesis yields and the masses of radioactive isotopes in the ejecta.

6.1. Ejecta of Hybrid C+O+Ne WD

6.1.1. Dependence on Central Density

In Figure 16, we plot $[X/^{56}\mathrm{Fe}]$ in the ejecta of the hybrid C +O+Ne WDs for models 100-043-1-c3, 300-047-1-c3, 500-048-1-c3, and 700-049-1-c3.

The abundance pattern of the ejecta is similar to the typical SN Ia. (1) IMEs are underproduced. (2) The V, Cr, Mn and Co isotopes are much higher in the higher central density models than the lower density models. (3) On the contrary, Fe and Ni isotopes are not sensitive to the central density except that ^{54}Fe and ^{58}Ni are higher for the higher central density. (4) Only in extreme cases such as Model 750-049-1-c3 we observe the

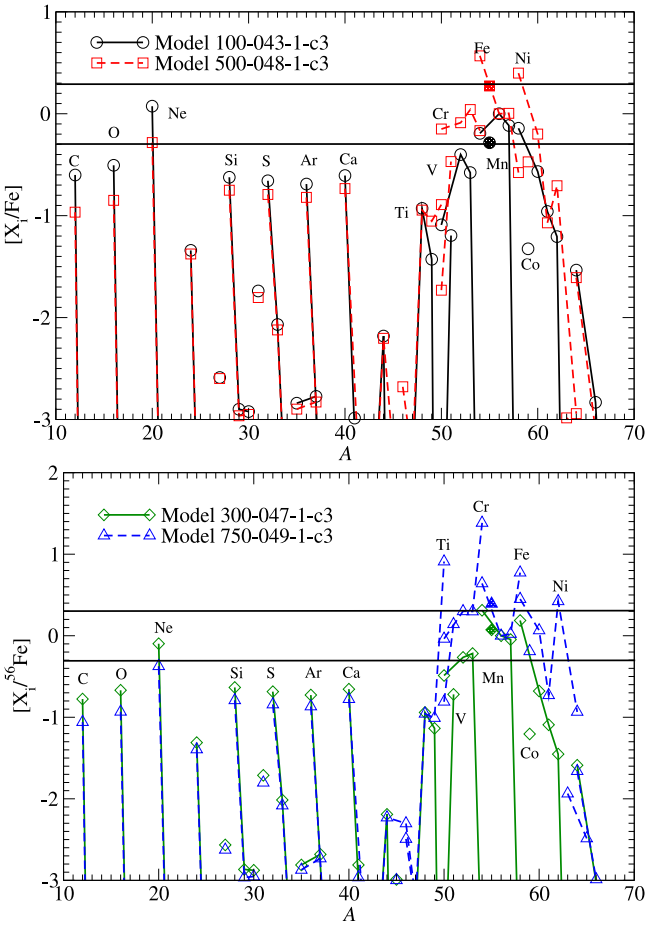

Figure 16. $[X_i/^{56}\mathrm{Fe}]$ against mass number for the ejecta of C+O WD models for models 100-043-1-c3 ($\rho_c = 1.0 \times 10^9$ g cm^{-3}) and 500-048-1-c3 ($\rho_c = 5.0 \times 10^9$ g cm^{-3}) in the top panel and 300-047-1-c3 ($\rho_c = 3.0 \times 10^9$ g cm^{-3}) and 750-049-1-c3 ($\rho_c = 7.5 \times 10^9$ g cm^{-3}) in the bottom panel. All models assume $X(^{22}\mathrm{Ne}) = 0.025$ and $c3$ initial flame.

severe overproduction of the neutron-rich isotopes ^{50}Ti, ^{54}Cr, ^{58}Fe and ^{62}Ni. (5) A growth of Mn with increasing central density is still seen but it saturates at a value [Mn/Fe] $\sim$ 2, while [Co/Fe] becomes compatible with the solar value.

The overall trend is similar to C+O WD models. The C+O+Ne composition only provides a lower-energy release due to the lower abundance of ^{12}C and higher abundance of ^{20}Ne. The C+O+Ne composition also makes the laminar flame propagation slower. In general, the turbulent flame dominates the flame propagation, which is independent of the composition. But the composition affects the turbulent flame indirectly by its energy feedback, which changes the turbulent motion inside the star, and hence the production and decay of turbulent motion.

In general, the CO deflagration does not differ much from the CONe deflagration at high density because in both cases, matter is burned into NSE. By comparing Figure 16 with Figure 8, the overall patterns suggest that, indeed, the properties of CO and CONe deflagration do not differ much except for minor details, such as the minor isotopes in IMEs and lower-mass iron-peak elements. But we remind the reader that a hybrid CONe WD takes a longer time for the deflagration wave to spread and burn to release the necessary energy for the expansion. This also means that the momentum transport from the hot ash to the cold fuel is slower.

Table 5
Mass of Major Isotopes in the Ejecta after All Short-lived Radioactive Isotopes Have Decayed

Isotopes	100-043-1-c3	200-045-1-c3	300-047-1-c3	500-048-1-c3	550-048-1-c3	750-049-1-c3	900-050-1-c3
^{12}C	1.32×10^{-1}	1.39×10^{-1}	1.34×10^{-1}	1.18×10^{-1}	1.23×10^{-1}	1.4×10^{-1}	9.35×10^{-2}
^{13}C	7.21×10^{-12}	1.95×10^{-11}	2.42×10^{-11}	3.0×10^{-11}	2.20×10^{-11}	3.16×10^{-11}	2.63×10^{-11}
^{14}N	2.76×10^{-9}	7.6×10^{-9}	8.29×10^{-9}	1.1×10^{-8}	7.29×10^{-9}	1.7×10^{-8}	1.8×10^{-8}
^{15}N	3.31×10^{-7}	5.52×10^{-7}	5.86×10^{-7}	6.42×10^{-7}	5.66×10^{-7}	7.33×10^{-7}	8.57×10^{-7}
^{16}O	3.63×10^{-1}	3.92×10^{-1}	3.80×10^{-1}	3.41×10^{-1}	3.52×10^{-1}	3.8×10^{-1}	2.85×10^{-1}
^{17}O	6.1×10^{-11}	1.67×10^{-10}	2.4×10^{-10}	2.53×10^{-10}	1.77×10^{-10}	2.54×10^{-10}	2.30×10^{-10}
^{18}O	2.89×10^{-12}	7.78×10^{-12}	9.52×10^{-12}	1.16×10^{-11}	8.20×10^{-12}	1.17×10^{-11}	1.5×10^{-11}
^{19}F	1.8×10^{-10}	2.68×10^{-10}	3.24×10^{-10}	4.1×10^{-10}	2.88×10^{-10}	4.1×10^{-10}	3.74×10^{-10}
^{20}Ne	2.16×10^{-1}	2.29×10^{-1}	2.22×10^{-1}	1.97×10^{-1}	2.5×10^{-1}	1.75×10^{-1}	1.57×10^{-1}
^{21}Ne	4.79×10^{-9}	1.6×10^{-8}	1.28×10^{-8}	1.57×10^{-8}	1.17×10^{-8}	1.55×10^{-8}	1.64×10^{-8}
^{22}Ne	8.38×10^{-9}	1.74×10^{-8}	2.6×10^{-8}	2.52×10^{-8}	1.96×10^{-8}	2.49×10^{-8}	2.79×10^{-8}
^{23}Na	2.68×10^{-6}	4.68×10^{-6}	5.61×10^{-6}	6.65×10^{-6}	5.65×10^{-6}	6.72×10^{-6}	7.73×10^{-6}
^{24}Mg	3.61×10^{-3}	5.60×10^{-3}	5.90×10^{-3}	6.90×10^{-3}	5.75×10^{-3}	7.22×10^{-3}	7.65×10^{-3}
^{25}Mg	8.84×10^{-8}	1.64×10^{-7}	1.92×10^{-7}	2.30×10^{-7}	1.86×10^{-7}	2.28×10^{-7}	2.58×10^{-7}
^{26}Mg	7.73×10^{-7}	1.34×10^{-6}	1.61×10^{-6}	1.89×10^{-6}	1.72×10^{-6}	1.93×10^{-6}	2.22×10^{-6}
^{26}Al	2.49×10^{-29}	2.88×10^{-29}	2.99×10^{-29}	4.65×10^{-28}	3.27×10^{-29}	4.44×10^{-28}	3.45×10^{-29}
^{27}Al	2.34×10^{-5}	3.45×10^{-5}	3.76×10^{-5}	4.74×10^{-5}	3.91×10^{-5}	4.87×10^{-5}	4.57×10^{-5}
^{28}Si	2.42×10^{-2}	3.40×10^{-2}	3.61×10^{-2}	3.76×10^{-2}	3.36×10^{-2}	3.73×10^{-2}	3.66×10^{-2}
^{29}Si	6.79×10^{-6}	1.11×10^{-5}	1.11×10^{-5}	1.21×10^{-5}	1.6×10^{-5}	1.32×10^{-5}	1.55×10^{-5}
^{30}Si	4.38×10^{-6}	6.99×10^{-6}	7.42×10^{-6}	8.52×10^{-6}	7.17×10^{-6}	9.24×10^{-6}	1.3×10^{-5}
^{31}P	1.45×10^{-5}	2.23×10^{-5}	2.35×10^{-5}	2.59×10^{-5}	2.22×10^{-5}	2.84×10^{-5}	2.95×10^{-5}
^{32}S	1.32×10^{-2}	1.78×10^{-2}	1.89×10^{-2}	2.1×10^{-2}	1.80×10^{-2}	1.95×10^{-2}	1.81×10^{-2}
^{33}S	4.24×10^{-6}	7.37×10^{-6}	7.31×10^{-6}	7.78×10^{-6}	6.87×10^{-6}	9.28×10^{-6}	1.19×10^{-5}
^{34}S	1.75×10^{-7}	3.7×10^{-7}	3.61×10^{-7}	4.0×10^{-7}	3.34×10^{-7}	5.5×10^{-7}	6.83×10^{-7}
^{36}S	2.84×10^{-13}	4.9×10^{-13}	4.78×10^{-13}	3.15×10^{-12}	4.30×10^{-12}	1.32×10^{-10}	3.94×10^{-10}
^{35}Cl	7.15×10^{-7}	1.6×10^{-6}	1.16×10^{-6}	1.29×10^{-6}	1.13×10^{-6}	1.50×10^{-6}	1.66×10^{-6}
^{37}Cl	2.86×10^{-7}	5.3×10^{-7}	5.38×10^{-7}	5.22×10^{-7}	5.7×10^{-7}	7.12×10^{-7}	8.88×10^{-7}
^{36}Ar	2.59×10^{-3}	3.45×10^{-3}	3.63×10^{-3}	3.98×10^{-3}	3.56×10^{-3}	3.90×10^{-3}	3.58×10^{-3}
^{38}Ar	2.42×10^{-8}	4.18×10^{-8}	4.88×10^{-8}	6.49×10^{-8}	6.66×10^{-8}	1.13×10^{-7}	1.48×10^{-7}
^{40}Ar	7.5×10^{-17}	1.28×10^{-16}	1.49×10^{-16}	4.89×10^{-13}	7.4×10^{-13}	1.45×10^{-11}	3.79×10^{-11}
^{39}K	1.29×10^{-7}	1.82×10^{-7}	1.99×10^{-7}	2.43×10^{-7}	2.17×10^{-7}	2.80×10^{-7}	3.28×10^{-7}
^{40}K	9.7×10^{-14}	1.67×10^{-13}	1.94×10^{-13}	3.55×10^{-13}	3.70×10^{-13}	6.85×10^{-13}	1.1×10^{-12}
^{41}K	4.3×10^{-8}	7.64×10^{-8}	9.20×10^{-8}	7.1×10^{-8}	8.9×10^{-8}	9.62×10^{-8}	1.3×10^{-7}
^{40}Ca	2.37×10^{-3}	3.10×10^{-3}	3.23×10^{-3}	3.66×10^{-3}	3.29×10^{-3}	3.62×10^{-3}	3.28×10^{-3}
^{42}Ca	1.38×10^{-10}	2.44×10^{-10}	3.59×10^{-10}	3.81×10^{-9}	4.8×10^{-9}	7.81×10^{-9}	1.1×10^{-8}
^{43}Ca	2.18×10^{-9}	2.30×10^{-9}	2.52×10^{-9}	3.38×10^{-9}	2.80×10^{-9}	3.35×10^{-9}	7.76×10^{-9}
^{44}Ca	1.47×10^{-6}	2.4×10^{-6}	2.20×10^{-6}	2.91×10^{-6}	2.55×10^{-6}	2.99×10^{-6}	2.93×10^{-6}
^{46}Ca	1.36×10^{-23}	5.99×10^{-22}	4.97×10^{-22}	3.4×10^{-11}	4.80×10^{-11}	4.23×10^{-9}	2.3×10^{-8}
^{48}Ca	1.84×10^{-25}	2.13×10^{-25}	2.21×10^{-25}	1.41×10^{-12}	3.0×10^{-12}	3.45×10^{-9}	6.64×10^{-7}
^{45}Sc	3.18×10^{-9}	6.8×10^{-9}	8.62×10^{-9}	1.4×10^{-8}	1.5×10^{-8}	1.25×10^{-8}	1.34×10^{-8}
^{46}Ti	7.17×10^{-9}	2.27×10^{-8}	3.85×10^{-8}	1.50×10^{-7}	1.58×10^{-7}	2.52×10^{-7}	3.5×10^{-7}
^{47}Ti	6.93×10^{-9}	1.15×10^{-8}	1.53×10^{-8}	2.77×10^{-8}	2.66×10^{-8}	3.74×10^{-8}	5.16×10^{-8}
^{48}Ti	3.97×10^{-5}	5.47×10^{-5}	5.89×10^{-5}	7.91×10^{-5}	7.27×10^{-5}	8.43×10^{-5}	8.19×10^{-5}
^{49}Ti	9.54×10^{-7}	2.4×10^{-6}	2.85×10^{-6}	4.68×10^{-6}	4.48×10^{-6}	5.67×10^{-6}	8.63×10^{-6}
^{50}Ti	1.18×10^{-19}	8.2×10^{-15}	7.8×10^{-15}	6.73×10^{-6}	1.0×10^{-5}	4.65×10^{-4}	1.89×10^{-3}
^{50}V	3.45×10^{-13}	2.17×10^{-12}	4.39×10^{-12}	4.64×10^{-9}	7.17×10^{-9}	4.23×10^{-8}	7.73×10^{-8}
^{51}V	3.25×10^{-6}	9.61×10^{-6}	1.48×10^{-5}	3.59×10^{-5}	3.82×10^{-5}	1.60×10^{-4}	3.45×10^{-4}

Note. The isotope masses are in units of solar mass.

6.1.2. Dependence on Initial Flame Structure

We examine the effects of the initial flame structure on the nucleosynthesis yield for the C+O+Ne WDs. In Figure 17, we plot $[X_i/^{56}\mathrm{Fe}]$ of the ejecta for models 300-047-1-c3 and 300-047-1-b1. The two WD models share the same configuration but with different initial flame geometry (centered flame *c*3 versus off-center flame *b*1).

As a demonstration, we compare the final nucleosynthesis yields of the ejecta in models 300-047-1-c3 and 300-047-1-b1 in the top panel and 750-049-1-c3 and 750-049-1-b1 in the bottom panel. The two models differ by the initial flame, where one is the central *c*3 flame and the other is the off-center *b*1 flame. The ejecta composition is very similar in both cases in the light elements of O, Ne, and IMEs such as Si, S, Ar, and Ca. Off-center flame gives a slightly lower or a comparable amount of C, O, Ne and IMEs. The difference of the flame mostly affects the iron-peak elements. In the lower-density models, the off-center flame tends to produce more Cr, Fe, Mn, and Ni with very significant overproduction. Strong enhancement of ^{59}Co for the *b*1 flame model can be seen. This is because the iron-peak elements, which are produced in the core region, can be transported more easily by the flame bubble that flows with buoyancy. On the other hand, iron-peak elements produced in the central region tend to fall back when they transport their momentum to outer fluid elements. In the

Table 6
(cont'd) Mass of Major Isotopes in the Ejecta after All Short-lived Radioactive Isotopes Have Decayed

Isotopes	100-043-1-c3	200-045-1-c3	300-047-1-c3	500-048-1-c3	550-048-1-c3	750-049-1-c3	900-050-1-c3
^{50}Cr	8.78×10^{-6}	3.0×10^{-5}	5.36×10^{-5}	1.58×10^{-4}	1.65×10^{-4}	2.24×10^{-4}	2.51×10^{-4}
^{52}Cr	8.67×10^{-4}	1.47×10^{-3}	1.80×10^{-3}	3.69×10^{-3}	4.2×10^{-3}	9.85×10^{-3}	1.48×10^{-2}
^{53}Cr	6.70×10^{-5}	1.64×10^{-4}	2.34×10^{-4}	5.77×10^{-4}	6.3×10^{-4}	1.13×10^{-3}	1.66×10^{-3}
^{54}Cr	4.87×10^{-11}	2.61×10^{-9}	5.32×10^{-9}	9.13×10^{-5}	1.32×10^{-4}	3.53×10^{-3}	1.13×10^{-2}
^{55}Mn	1.5×10^{-3}	2.52×10^{-3}	3.64×10^{-3}	7.85×10^{-3}	7.93×10^{-3}	1.13×10^{-2}	1.37×10^{-2}
^{54}Fe	7.18×10^{-3}	2.6×10^{-2}	3.50×10^{-2}	8.58×10^{-2}	8.94×10^{-2}	1.11×10^{-1}	1.18×10^{-1}
^{56}Fe	1.82×10^{-1}	2.42×10^{-1}	2.78×10^{-1}	3.78×10^{-1}	3.55×10^{-1}	4.13×10^{-1}	4.56×10^{-1}
^{57}Fe	3.40×10^{-3}	4.99×10^{-3}	6.8×10^{-3}	9.29×10^{-3}	8.86×10^{-3}	1.5×10^{-2}	1.18×10^{-2}
^{58}Fe	1.19×10^{-10}	8.82×10^{-9}	2.6×10^{-8}	3.73×10^{-4}	5.34×10^{-4}	9.16×10^{-3}	2.45×10^{-2}
^{60}Fe	2.71×10^{-26}	9.96×10^{-22}	6.64×10^{-22}	5.21×10^{-10}	7.15×10^{-10}	9.73×10^{-8}	6.26×10^{-6}
^{59}Co	2.43×10^{-5}	3.38×10^{-5}	4.88×10^{-5}	3.59×10^{-4}	3.94×10^{-4}	7.49×10^{-4}	9.97×10^{-4}
^{58}Ni	5.35×10^{-3}	1.10×10^{-2}	1.74×10^{-2}	3.85×10^{-2}	4.0×10^{-2}	4.74×10^{-2}	4.96×10^{-2}
^{60}Ni	8.3×10^{-4}	8.46×10^{-4}	9.47×10^{-4}	3.88×10^{-3}	4.17×10^{-3}	7.81×10^{-3}	1.0×10^{-2}
^{61}Ni	1.50×10^{-5}	1.54×10^{-5}	1.69×10^{-5}	2.42×10^{-5}	2.36×10^{-5}	5.79×10^{-5}	1.9×10^{-4}
^{62}Ni	2.67×10^{-5}	2.24×10^{-5}	2.30×10^{-5}	1.74×10^{-4}	2.40×10^{-4}	2.56×10^{-3}	5.86×10^{-3}
^{64}Ni	7.9×10^{-18}	2.33×10^{-15}	3.55×10^{-15}	3.9×10^{-7}	4.61×10^{-7}	3.44×10^{-5}	5.98×10^{-4}
^{63}Cu	6.64×10^{-8}	6.7×10^{-8}	7.31×10^{-8}	1.99×10^{-7}	2.37×10^{-7}	2.43×10^{-6}	1.1×10^{-5}
^{65}Cu	3.87×10^{-8}	4.7×10^{-8}	4.43×10^{-8}	6.7×10^{-8}	5.74×10^{-8}	3.17×10^{-7}	1.49×10^{-6}
^{64}Zn	4.53×10^{-6}	5.42×10^{-6}	6.10×10^{-6}	7.93×10^{-6}	6.72×10^{-6}	7.68×10^{-6}	8.76×10^{-6}
^{66}Zn	1.34×10^{-7}	1.18×10^{-7}	1.28×10^{-7}	1.44×10^{-7}	1.27×10^{-7}	2.12×10^{-7}	8.84×10^{-6}
^{67}Zn	2.17×10^{-10}	2.81×10^{-10}	3.13×10^{-10}	4.43×10^{-10}	3.83×10^{-10}	2.51×10^{-9}	4.56×10^{-7}
^{68}Zn	7.61×10^{-9}	1.19×10^{-8}	1.26×10^{-8}	1.77×10^{-8}	1.56×10^{-8}	3.61×10^{-8}	2.6×10^{-7}
^{70}Zn	1.94×10^{-27}	7.30×10^{-27}	7.19×10^{-27}	2.29×10^{-14}	3.85×10^{-14}	2.38×10^{-11}	2.88×10^{-8}

Note. The isotope masses are in units of solar mass.

Table 7
Masses of the Radioactive Isotopes in the Ejecta after the Explosion

Isotopes	100-043-1-c3	200-045-1-c3	300-047-1-c3	500-048-1-c3	550-048-1-c3	750-049-1-c3	900-050-1-c3
^{22}Na	7.3×10^{-9}	1.43×10^{-8}	1.69×10^{-8}	2.5×10^{-8}	1.59×10^{-8}	2.2×10^{-8}	2.27×10^{-8}
^{26}Al	6.45×10^{-7}	1.10×10^{-6}	1.32×10^{-6}	1.55×10^{-6}	1.35×10^{-6}	1.58×10^{-6}	1.84×10^{-6}
^{39}Ar	7.45×10^{-16}	1.26×10^{-15}	1.47×10^{-15}	4.96×10^{-14}	7.28×10^{-14}	5.30×10^{-13}	1.4×10^{-12}
^{40}K	9.12×10^{-14}	1.68×10^{-13}	1.95×10^{-13}	3.57×10^{-13}	3.72×10^{-13}	6.89×10^{-13}	1.1×10^{-12}
^{41}Ca	3.69×10^{-8}	6.54×10^{-8}	7.86×10^{-8}	7.11×10^{-8}	7.61×10^{-8}	9.73×10^{-8}	1.4×10^{-7}
^{44}Ti	1.48×10^{-6}	2.1×10^{-6}	2.17×10^{-6}	2.71×10^{-6}	2.44×10^{-6}	2.80×10^{-6}	2.73×10^{-6}
^{48}V	5.9×10^{-10}	9.69×10^{-10}	1.32×10^{-9}	2.54×10^{-9}	2.54×10^{-9}	3.17×10^{-9}	3.51×10^{-9}
^{49}V	6.40×10^{-11}	2.53×10^{-10}	4.74×10^{-10}	4.2×10^{-8}	5.36×10^{-8}	1.35×10^{-7}	1.99×10^{-7}
^{53}Mn	9.19×10^{-8}	1.16×10^{-6}	3.15×10^{-6}	2.23×10^{-4}	2.58×10^{-4}	5.35×10^{-4}	7.8×10^{-4}
^{60}Fe	1.32×10^{-25}	1.47×10^{-20}	9.87×10^{-21}	7.47×10^{-9}	1.15×10^{-8}	1.39×10^{-6}	9.9×10^{-5}
^{56}Co	6.46×10^{-6}	1.81×10^{-5}	3.28×10^{-5}	8.57×10^{-5}	9.8×10^{-5}	1.11×10^{-4}	1.19×10^{-4}
^{57}Co	1.18×10^{-6}	1.6×10^{-5}	3.15×10^{-5}	8.72×10^{-4}	9.10×10^{-4}	1.59×10^{-3}	1.88×10^{-3}
^{60}Co	3.96×10^{-17}	2.68×10^{-14}	3.67×10^{-14}	4.90×10^{-8}	7.2×10^{-8}	9.86×10^{-7}	2.60×10^{-6}
^{56}Ni	1.82×10^{-1}	2.42×10^{-1}	2.78×10^{-1}	3.58×10^{-1}	3.30×10^{-1}	3.44×10^{-1}	3.56×10^{-1}
^{57}Ni	3.40×10^{-3}	4.98×10^{-3}	6.5×10^{-3}	8.37×10^{-3}	7.87×10^{-3}	8.38×10^{-3}	8.77×10^{-3}
^{59}Ni	2.8×10^{-6}	9.1×10^{-6}	2.21×10^{-5}	3.8×10^{-4}	3.18×10^{-4}	5.18×10^{-4}	5.91×10^{-4}
^{63}Ni	1.33×10^{-20}	6.32×10^{-16}	6.26×10^{-16}	5.77×10^{-8}	8.25×10^{-8}	1.94×10^{-6}	9.8×10^{-6}

Note. The isotope masses are in units of solar mass.

high-density models, not much difference in the pattern can be found. This is because the propagation becomes so rapid and energetic that the flame burns similarly and ejects most of the WD.

6.2. Remnant of Hybrid C+O+Ne WD

6.2.1. Dependence on Central Density

In Figure 18, we plot the abundance patterns of the bound remnants in models 100-043-1-c3, 300-047-1-c3, 500-048-1-c3, and 750-049-1-c3. This series of models studies the effects of the central density of the WD, on the chemical composition of the remnant.

Both panels show that the initial central density strongly influences the iron-peak elements in the remnant. A higher central density leads to a stronger enhancement of neutron-rich isotopes like ^{50}Ti, ^{54}Cr, ^{58}Fe, and ^{62}Ni. Their ratios to ^{56}Fe can be from 10 to 10,000 times the solar ratio. The trend can already be seen in the C+O WDs. Isotopes with $Y_e \approx 0.5$, for example, ^{46}Ti, ^{50}Cr, ^{54}Fe, and ^{58}Ni, share similar ratios

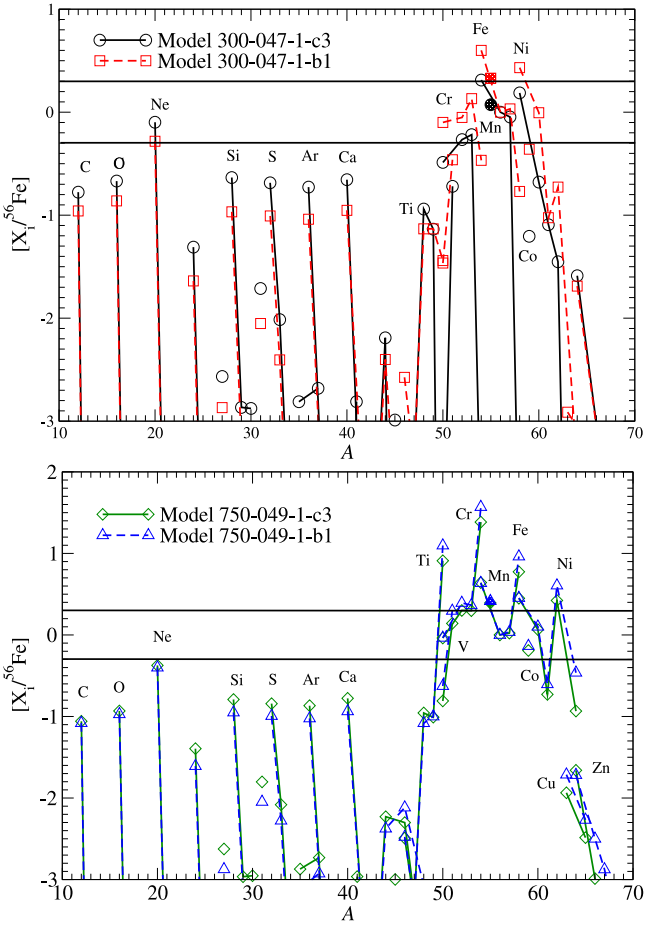

Figure 17. (Top panel) $[X_i/^{56}\mathrm{Fe}]$ against mass number for the ejecta in hybrid C+O+Ne WD models for 300-047-1-c3 ($c3$ flame) and 300-047-1-b1 ($b1$ flame). (Bottom panel) Same as the top panel but for models 750-049-1-c3 and 750-049-1-b1. All models assume $X(^{22}\mathrm{Ne}) = 0.025$ and $c3$ initial flame.

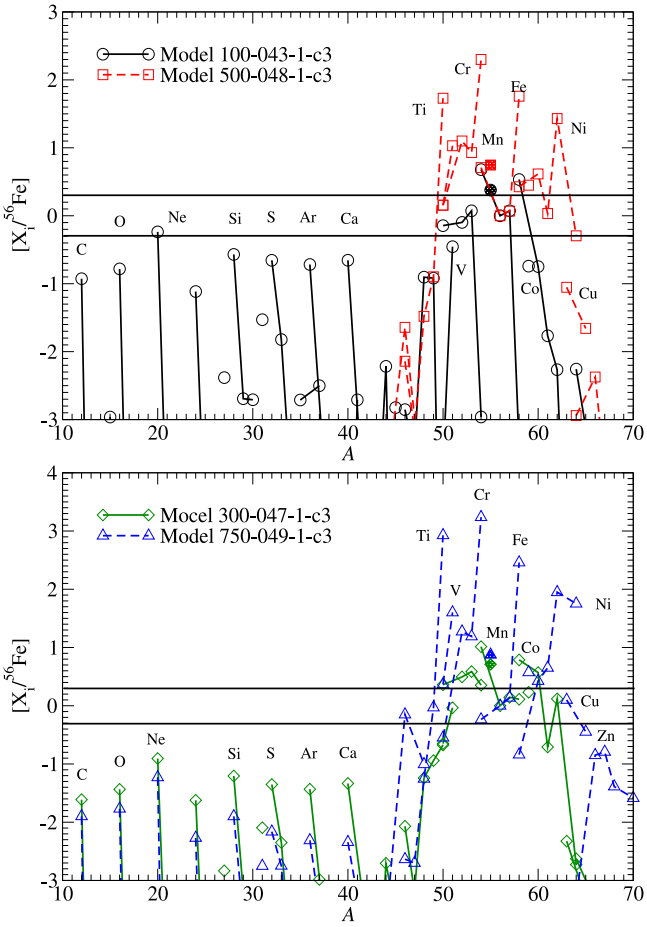

Figure 18. The $[X_i/^{56}\mathrm{Fe}]$ against mass number for the remnants of hybrid C+O+Ne WD models for models 100-043-1-c3 ($\rho_c = 1.0 \times 10^9$ g cm^{-3}) and 500-048-1-c3 ($\rho_c = 5.0 \times 10^9$ g cm^{-3}) in the top panel and 300-047-1-c3 ($\rho_c = 3.0 \times 10^9$ g cm^{-3}) and 750-049-1-c3 ($\rho_c = 7.5 \times 10^9$ g cm^{-3}) in the bottom panel. All models assume $X(^{22}\mathrm{Ne}) = 0.025$ and $c3$ initial flame.

among all models. This is consistent with our previous results that matter with a higher density has a faster electron-capture rate, which strongly favors the production of neutron-rich isotopes.

The general abundances of the IMEs (Si, S, Ar, Ca) drop when the progenitor mass increases. This is because as the mass increases, the star becomes more compact, and the density drop in the outer part becomes steeper. Thus, there is a lower mass of matter with a low density ($\sim 10^7$ g cm^{-3}). One exception is in model 500-048-1-c3. In that model, no CONe C+O+Ne-rich matter or IMEs can be found. This feature is comparable with model 800-139-1-c3. The nonmonotonic trend suggests that the fallback event is sensitive to how outer matter is ejected. However, we remind the reader that even the IME abundances are higher in model 800-049-1-c3; it is only about a few percent of the solar values.

Despite some isotopes being extremely overproduced compared to the solar ratio, we remind the reader that their corresponding masses as a part of the element can still be smaller or only comparable with the major isotopes of their corresponding elements. In particular, in spectrography, the atomic lines are sensitive to the elements but not individual isotopes.

6.2.2. Dependence on Initial Flame Structure

In Figure 19, we compare the chemical composition of the remnant in models 300-047-1-c3 and 300-047-1-b1 in the top panel and 750-049-1-c3 and 750-049-1-b1 in the bottom panel. The two models differ by the initial flame.

In the low-density models, the remnant composition is characterized by a significant overproduction of iron-peak elements. Larger amounts of C+O+Ne-rich matter and IMEs can be observed, again suggesting that an off-center flame helps to eject matter more easily due to weaker gravitational attraction and less matter on top of burned matter. On the other hand, a flame farther from the center produces ash that has experienced less electron capture before it cools down. The difference can be seen in the abundance of neutron-rich isotopes ^{54}Cr, ^{58}Fe, ^{59}Co, and ^{62}Ni. Apart from that, the pattern of iron-peak elements is similar.

Then we also compare the abundance yields using different initial flames for the high-density models. The abundance pattern is less sensitive to the initial flame structures. The CONe-rich matter and IMEs are higher in the off-center flame model (750-049-1-b1), while there is a higher abundance of iron-peak elements in the centered flame model (750-049-1-c3).

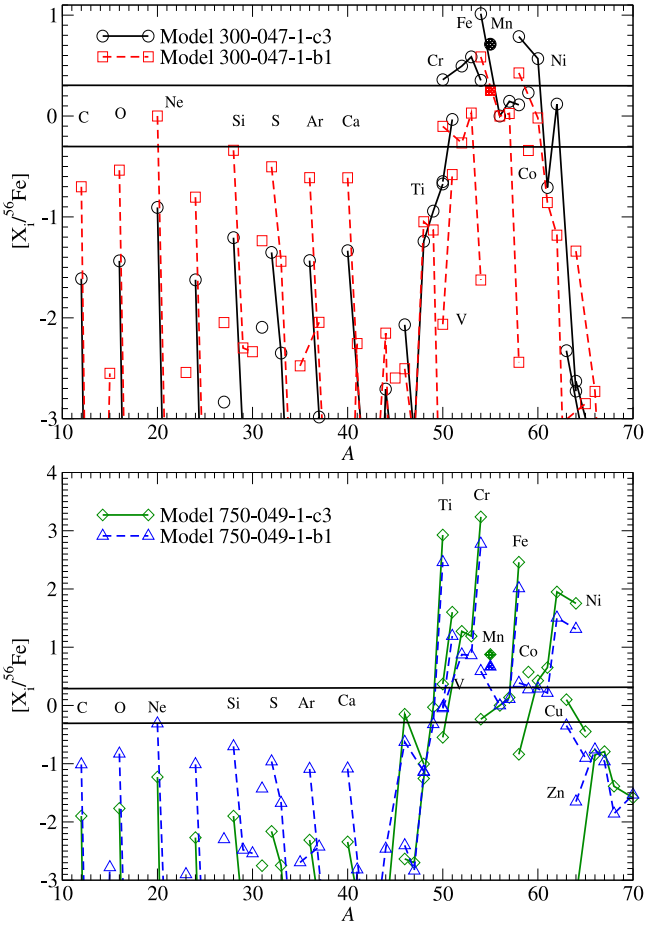

Figure 19. (top panel) $[X_i/^{56}\mathrm{Fe}]$ against atomic mass for the remnants of hybrid CO+ONe WD models for models 300-047-1-c3 (*c*3 flame) and 300-047-1-b1 (*b*1 flame). (Bottom panel) Similar to the top panel but for 750-049-1-c3 (*c*3 flame) and 750-049-1-b1 (*b*1 flame). All models assume $X(^{22}\mathrm{Ne}) = 0.025$ and C/O ratio = 1.

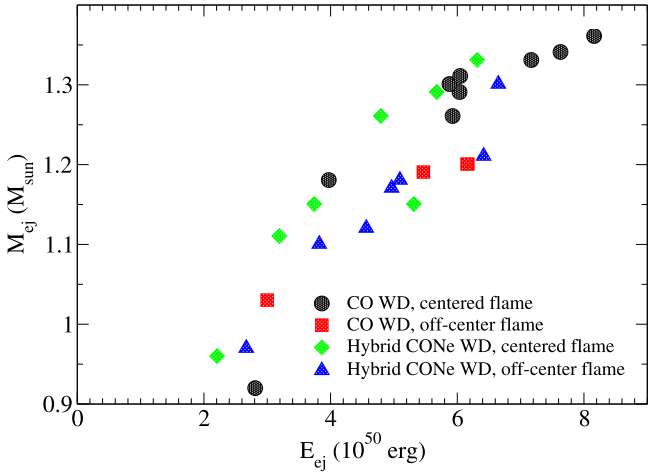

Figure 20. Ejecta mass against final WD ejecta energy for all models in this work.

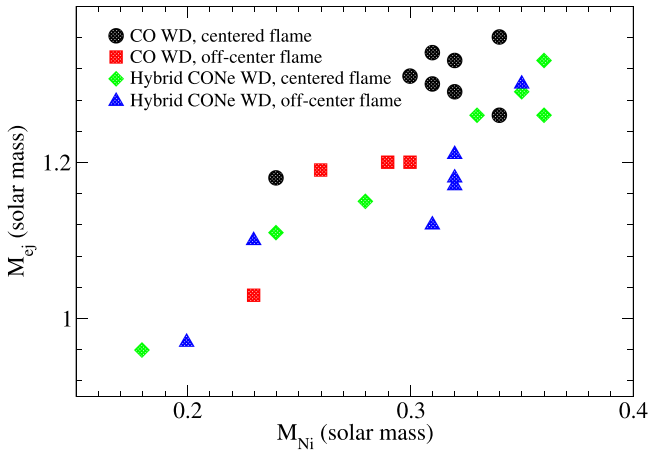

Figure 21. Ejecta mass against ejected ^{56}Ni mass for all models in this work.

7. Discussion

7.1. Ejecta and Its Observable

7.1.1. Ejecta Mass–Ejecta Energy Relation

In observing SNe Iax, the parameter space ($M_{\rm ej}$, $E_{\rm ej}$), i.e., the pair of ejecta mass and ejecta energy, is important owing to the presence of a bounded remnant.

To derive this relation, we collect the final kinetic energy of the ejecta, together with their total mass. In Figure 20, we plot the ejecta mass against the WD final energy for the models presented in this work. We can see that a clear monotonic trend appears where the higher final energy corresponds to a higher ejecta mass. A quasi-linear relation can be seen for $E_{\rm ej} < 6 \times 10^{50}$ erg. For $E_{\rm ej}$ greater than that, the data approach the asymptotic value of $\sim 1.4\,M_\odot$ and level off.

We further fit the data points with a linear relation at low $E_{\rm ej}$. We observe a linear relation for $E_{\rm ej}$ in the range (2–6) $\times 10^{50}$ erg as $M_{\rm ej} = 0.9 + 0.1E_{\rm ej}$ with a χ^2 of about 0.28. However, we expect that the linear relation will break down in the low-$E_{\rm ej}$ limit as it corresponds to the limit where the ejecta has no energy, meaning that no ejecta exists. In that case, the relation should fall steeply toward the origin.

7.1.2. Ejecta Mass–^{56}Ni Mass Relation

The ejecta mass–^{56}Ni mass relation provides a test of how explosion strength is connected to the light-curve feature. In general, the ejecta mass is related to the width, and the ^{56}Ni mass is related to the width and peak luminosity of the light curve. We plot in Figure 21 the ejecta mass against ^{56}Ni for all models we presented in this work. Each group of SN Iax models has its own slope due to the different ways to explode the star and the corresponding energy production. For example, the data for the C+O WD models with a centered flame are more clustered near $M_{\rm Ni} = 0.3$. This is because those data points correspond to where the star is almost completely disrupted, while the lack of detonation bounds the possible ^{56}Ni production.

However, globally, the models show a general linear trend with dispersion. We again see that at low ^{56}Ni, the pair has a linear relation to a good approximation, which can be fitted by $M_{\rm ej} \approx 4M_{\rm Ni}$ where we require the fitting line to pass through the origin.

Accompanying with the partial ejection of the WD materials, a small mass WD, which is bounded gravitationally, survives. The typical bounded mass ranges from 0.2 to 1.1 $M_\odot$, depending on the explosion strength. Such a WD remnant is

observable. The WDs of mass $\sim 0.3\ M_\odot$ are observed (see, e.g., Brown et al. 2010).

7.1.3. ^{56}Ni Mass–Ejecta Velocity Relation

At last, we examine the ejecta velocity relation with ^{56}Ni production ($M_{\rm Ni}$). These two quantities are associated with the observable pair Si II Velocity against absolute magnitude at peak M_V. In Figure 22, we plot the ejecta ^{56}Ni against ejecta characteristic velocity. The velocity of the ejecta $v_{\rm ejecta}$ is computed by first summing up the kinetic energy E_k of all tracer particles, and then we obtain $v_{\rm ejecta} = \sqrt{2E_k/M_{\rm ej}}$.

We observe in this pair of observables that the ejecta velocity linearly increases with ^{56}Ni mass. The typical ejecta velocity ranges between 5000 and 8000 km s^{-1}. This corresponds to models with a strong explosion when M is large, where the energy production increases more rapidly than the growth of mass. For a given ejecta velocity, it can correspond a dispersion of ^{56}Ni mass of $\sim 0.1\ M_\odot$ in the high-velocity limit, and the dispersion is smaller otherwise. This "fan"-shaped pattern allows more diversity of SNe Iax when they are more luminous.

However, in this figure, we do not attempt to directly compare our theoretical models with the observational data, such as those in Foley et al. (2013). This is because, to extract a reliable estimation of Si II velocity, the photosphere position and the corresponding velocity of the Si shell are essential. The exact value can be obtained by directly carrying out radiative transfer. To further relate the expected peak luminosity with the ^{56}Ni production, radiative transfer with gamma-ray energy deposition is necessary for a consistent prediction.

7.1.4. Ejecta Elemental Abundance

In typical spectral observations of SNe Iax and their remnants, the elemental abundances are measured instead of the isotopic abundances. Here we examine how the chemical abundance of SNe Iax depends on the progenitor mass. By using the postdecay (i.e., after 10^6 yr) stable isotopic contributions in the ejecta, we sum the mass of the isotopes of each element from C to Zn, then we compute the corresponding [Z/Fe] for models 100-133-1-c3-1 ($\rho_c = 1 \times 10^9$ g cm^{-3}), 300-137-1-c3-1 ($\rho_c = 3 \times 10^9$ g cm^{-3}), 500-138-1-c3-1 ($\rho_c = 5 \times 10^9$ g cm^{-3}), and 800-139-1-c3-1 ($\rho_c = 9 \times 10^9$ g cm^{-3}). We remind the reader that minor long-lived radioactive isotopes still contribute, but their amounts are much smaller than the major stable isotopes. These models correspond to models with different central densities and hence different progenitor masses.

In Figure 23, we plot the element abundances of these models. The ejecta composition after fallback, when the hot ash pushes the external envelope and atmosphere away from the WD, appears to have a similar abundance pattern. Except for model 800-139-1-c3-1, the other models share features, including subsolar IMEs with similar ratios of [Ca/S]. Light IMEs are also underproduced. This is because the turbulent flame is subsonic, which cannot follow the pace of expanding matter for creating an adequate amount of IMEs. The ejecta features an abundant amount of Mn, Fe, and Ni with respect to the solar composition. For the contrasting model 800-139-1-c3-1, it shows a much higher Ti, V, and Cr. Such a difference can be the key to identifying the difference in progenitors from future SNR observations.

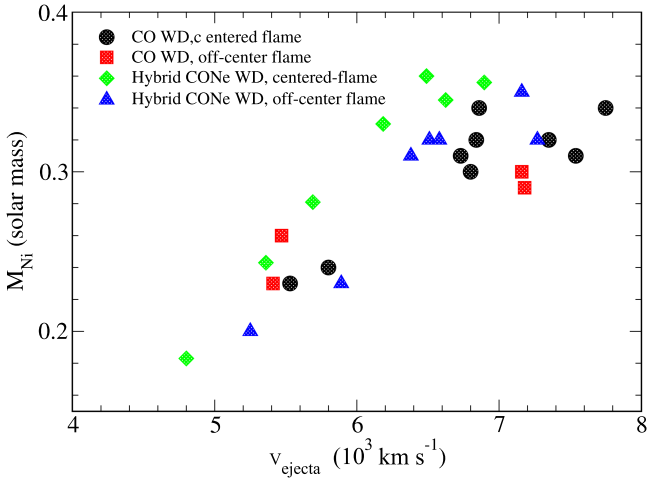

Figure 22. Ejecta ^{56}Ni mass against ejecta characteristic velocity for the SN Iax models presented in this work.

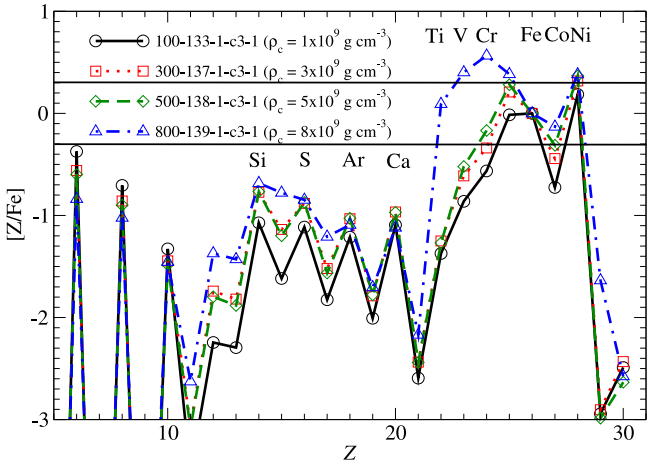

Figure 23. Ejecta chemical abundance [Z/Fe] against Z for models 100-133-1-c3-1 ($\rho_c = 1 \times 10^9$ g cm^{-3}), 300-137-1-c3-1 ($\rho_c = 3 \times 10^9$ g cm^{-3}), 500-138-1-c3-1 ($\rho_c = 5 \times 10^9$ g cm^{-3}), and 800-139-1-c3-1 ($\rho_c = 8 \times 10^9$ g cm^{-3}). All models assume C+O WD, $c3$ flame, $X(^{22}\mathrm{Ne}) = 0.025$, and C/O mass fraction ratio = 1.

7.2. Application to Observed Low-mass WDs

In Raddi et al. (2018, 2019), the abundance patterns are extracted from the spectra of some low-mass WDs with unusually high metal fractions. They are also traveling with a high velocity. They include LP 40-365, J1603–6613, and J1825–3757.

In Figure 24, we plot the abundance patterns of these objects, together with some of our representative models presented in this work. To obtain the final chemical composition, after the remnant chemical composition is obtained by postprocessing, the composition in the remnant is assumed to be completely mixed. We allow the remnant to pass $\sim 10^6$ yr until most typical radioactive elements have completely decayed. Exceptions include very long-lived radioactive elements, such as ^{27}Al and ^{60}Fe. In this work, when the radioactive decay injects energy into the remnant, the remnant is assumed to be static. No mass loss is assumed in this process.

The models include 500-138-1-c3-1, 500-05-1-c3-1, 900-140-1-c3-1, and 900-050-1-c3-1. The first two models correspond to the C+O and hybrid C+O+Ne WD models with $\rho_c = 5 \times 10^9$ g cm^{-3}. The last two models correspond to the C+O and hybrid C+O+Ne WDs with $\rho_c = 9 \times 10^9$ g cm^{-3}.

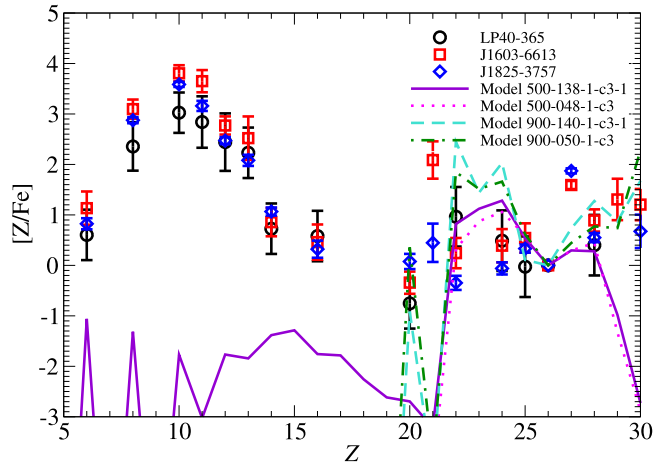

Figure 24. Abundance patterns [Z/Fe] of low-mass WDs, including LP 40-365, J1603–6613, and J1825–3757. Representative SN Iax models including 500-138-1-c3-1, 500-047-1-c3-1, 900-140-1-c3-1, and 900-050-1-c3-1 are included for comparison.

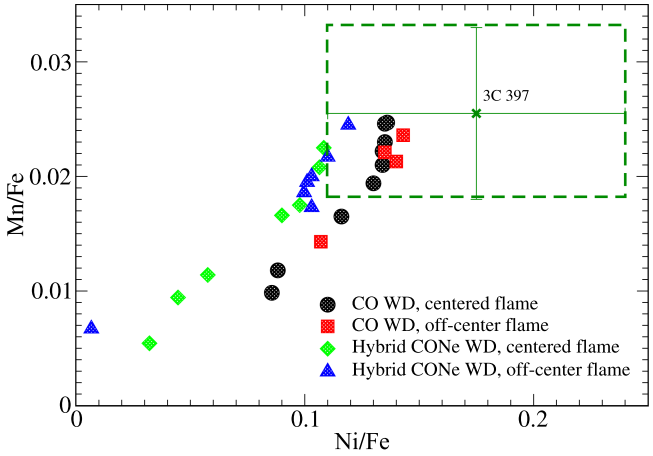

Figure 25. The mass ratios of Mn/Fe against Ni/Fe for the ejecta from C+O and hybrid C+O+Ne WD models in this work. The cross corresponds to the SNR 3C 397.

These observed WDs feature extremely abundant light elements, including C, O, Ne, Na, Mg, and Al. These are as high as 10^4 times the solar abundances with respect to Fe. The observed abundances of IMEs (Si, S, and Ca) in these WDs are comparable with the solar abundances. It would be interesting to note that these WDs have supersolar iron-peak elements, especially Mn, Co, and Ni.

Our models all show a systematic underproduction of light elements, none of which are supersolar. The IMEs are also too low compared to the objects. However, these features could originate from other reasons, e.g., the progenitors of the WDs. Possible later energy deposition due to the ^{56}Ni decay in the remnant can also trigger further mass loss, which may further lower the Fe contribution.

The iron-peak elements of our models appear to be similar to the observations. The values for Ti, Cr, and Ni are particularly close to the observed values. We remark that the ejecta of this model shows a much higher V, but not in the remnant WD. However, none of our models can reproduce the ∼100 times production of Co/Fe as seen in the two WDs shown here.

We note that there are SN Iax models without leaving a WD remnant. For example, Sahu et al. (2008) showed that the early and late time light curves and spectra of SN 2005hk are well-reproduced with the pure deflagration model which has no WD remnant.

Such weak explosion models can be found in PTD models with pulsation (e.g., Nomoto et al. 1976) and relatively fast flame propagation (e.g., Fink et al. 2014). The exact ejection mass depends strongly on the initial flame location. An off-center flame tends to suppress the ejected mass.

7.3. Application to SNRs

We further apply the explosion yield to some SNRs. In Yamaguchi et al. (2015), the chemical abundance pattern of the SNR 3C 397 is discussed. Similar analysis has been done for various SNRs in the galaxy and the Large Magellanic Cloud, as reported in Martínez-Rodríguez et al. (2017). From the X-ray spectra, it is found that this galactic SNR (3C 397) contains extremely high mass ratios Mn/Fe and Ni/Fe, which hints at the possibility of supersolar metallicity of the progenitor star.

However, in Dave et al. (2017), another possibility of using the Chandrasekhar mass model in the high-mass end ($\rho_c \sim 6 \times 10^9$ g cm^{-3}) is proposed to explain the high Mn/Ni mass ratio. Here we further investigate whether SN Iax models can approach this data point without invoking high metallicity. Also, in Martínez-Rodríguez et al. (2017), the Ca/S mass ratio can be the hint to understand the diversity of observed SNRs with the parameters other than metallicity. Here we examine how the central density of the WD contributes to the diversity.

In Figure 25, we plot the mass ratios Mn/Fe against Ni/Fe for models in Table 1. The cross corresponds to the SNR 3C 397 with the one sigma error box is shown. C+O WD models with $\rho_c > 6 \times 10^9$ g cm^{-3} are found in the observational error box. We remark that in PTD models, neutron-rich iron-peak elements are synthesized by the deflagration in the central region where Ye is determined by electron capture in NSE. Thus Mn/Fe and Ni/Fe are sensitive to the central Ye and thus the central density, but not the initial metallicity. In DDT models, on the other hand, iron-peak elements are produced (in addition to the central deflagration) in the detonation at the low density outer region, so that Mn/Fe and Ni/Fe are more sensitive to the initial Ye and thus metallicity.

In Yamaguchi et al. (2015), the Cr/Fe mass ratio is also measured as $0.027\pm^{0.007}_{0.006}$. By comparing with our chemical yields listed in Tables 3 and 6, Cr/Fe is sensitive to the central density as well. It sharply increases from ∼0.003 in model 100-133-1-c3-1 to ∼0.064 in model 900-140-1-c3-1. The best value lies around model 750-139-1-c3-1 as 0.029. Similar results appear for the hybrid C+O+Ne WD, which has a range of ∼0.005–0.045 in our sampled density range. Model 750-050-1-c3-1 again has a ratio 0.026, being closest to the observational data. The sharp dependence on the WD progenitor mass provides another precise indicator to identify the required numerical model. It suggests that treating Cr/Fe, Mn/Fe, and Ni/Fe as a three-dimensional parameter space can largely confine the potential SN Iax models as a physical origin of SNR 3C 397.

In order to judge if PTD is the origin of 3C 397, further constraints apply to this object, such as the mass ratios of Ca/S and Ar/S. The observed mass ratios are Ca/S = 0.12−0.16 and Ar/S = 0.17−0.18 (Martínez-Rodríguez et al. 2017). Our

models with $\rho_c \geqslant 5.5 \times 10^9\,\mathrm{g\,cm^{-3}}$ give the mass ratios of Ca/S = 0.08−0.16 and Ar/S = 0.14−0.17 for C+O WDs and Ca/S = 0.18−0.19 and Ar/S ∼ 0.20 for hybrid C+O+Ne WDs. The tight constraint by Ar/S is challenging to the claim that 3C 397 is an SN Iax origin. Future detection or no-detection of a low mass WD remnant will provide a definite indication to this physical picture.

Besides SNRs, the nucleosynthesis results presented in this work can be further applied to galactic chemical evolution (e.g., Matteucci & Greggio 1986; Pagel 1997; Kobayashi et al. 2020) to identify the role of individual types of SNe to the trend formation of specific elements as a function of metallicity. In particular, SNe Iax can be important in dSphs, where the star formation history can be very different from ordinary galaxies. The unique abundance pattern by SNe Iax can leave observable effects. For example, in models for dSph (Kobayashi et al. 2015, 2020; Cescutti & Kobayashi 2017), SNe Iax contribute to form the evolutionary trends of [Mn/Fe] and [O/Fe] consistently.

8. Conclusion

In this work, we have carried out the parameter survey for the explosive nucleosynthesis in SN Iax models using the PTD model as the explosion mechanism. We explored near-Chandrasekhar mass C+O WDs and hybrid C+O+Ne WDs as the progenitors. We studied nucleosynthesis products in both the ejecta and bound remnants and their parameter dependence, including the central density of the progenitor WD, initial flame structure, initial C/O ratio, and turbulent flame speed formula for the two types of WDs. Our results are summarized as follows.

(1) The ejecta is a mixture of burned ash with iron-peak elements and unburned C+O- or C+O+Ne-rich matter.
(2) The central density of the progenitor WD is the most important parameter for chemical compositions of the ejecta and the remnant WD. The explosion models with higher central densities enhance production of V, Cr, Fe, and Ni relative to Fe by up to ∼100 times the solar abundance in the ejecta and close to 10^3 times in the remnant WDs. The abundance in the ejecta is also sensitive to the initial flame structure. It is less sensitive to the C/O ratio and turbulent flame speed formula.
(3) The hybrid C+O+Ne WD shows similar features to the C+O WD except that the ejected mass is smaller due to the smaller nuclear energy release. The ejecta includes iron-peak elements with similar abundance patterns to the solar, while the remnant WD contains overproduced Ti, V, and Cr. In both ejecta and the remnant WD, IMEs such as Si, S, Ar, and Ca are underproduced.
(4) We compare the relations between the ejecta mass, explosion energy, and ^{56}Ni mass in our models. We find a linear trend for the low-energy explosion up to $\sim 4 \times 10^{50}$ erg and ^{56}Ni up to $\sim 0.3\,M_\odot$. We also examine the ^{56}Ni mass against the ejecta velocity to compare with the observational trends of SNe Iax. A clear linear trend can be observed for the ejecta mass against ejecta energy and ^{56}Ni mass in the ejecta.
(5) We further compare the model abundances with the recently observed low-mass WDs: LP 40-365, J1603–6613, and J1825–3757. Our models reproduce some aspects of the observed abundance pattern, especially the enhanced iron-peak elements. The observed high abundances of Cr, Mn, and Ni are consistent with an explosion at the central density as high as $\sim 5 \times 10^9\,\mathrm{g\,cm^{-3}}$. However, the high ratio of [Co/Fe] cannot be reproduced.
(6) We compare our yields with the recently observed SNR 3C 397, which has supersolar Mn/Fe and Ni/Fe ratios. Our models with a central density as high as $\sim 5 \times 10^9\,\mathrm{g\,cm^{-3}}$ reproduce the measured high Mn/Fe and Ni/Fe ratios. Thus SN Iax from a near Chandrasekhar mass WD with a high enough central density (and solar metallicity) is a possible alternative to the SN Ia with very high metallicity ($5\,Z_\odot$) (e.g., Leung & Nomoto 2018, 2020) for the model of 3C 397. However, further accurate determination of the observed abundances may be necessary to distinguish between models for 3C 397.

This work has been supported by the World Premier International Research Center Initiative (WPI Initiative), MEXT, Japan, and JSPS KAKENHI grant Nos. JP17K05382 and JP20K04024. S.C.L. also acknowledges support from the funding HST-AR-15021.001-A and 80NSSC18K1017.

We thank Francis Xavier Timmes for the open-source subroutines, including the Helmholtz equation of state, seven-isotope network, and torch nuclear reaction network. S.C.L. thanks Friedrich Roepke and Florian Lach for the insightful discussion on the topic of deflagration and flame geometry. We thank Chiaki Kobayashi for the motivation of this project from the galactic chemical evolution perspective. We thank Samuel Jones for useful discussions of nucleosynthesis. We thank Hiroya Yamaguchi for the detailed modeling of the SNR 3C 397.

Appendix A
Overview and Input Physics of the Simulation Code

In this section, we briefly review the input physics we use for modeling the SNe Iax in this article.

We use our own SN hydrodynamics code for all hydrodynamics simulations here. The code solves the two-dimensional Euler equations with a shock-capturing scheme. The spatial discretization is obtained by the fifth-order, weighted, essentially nonoscillatory scheme (Barth & Deconinck 1999), and the time discretization is obtained by the five-step, third-order, non-strong, stability-preserving Runge–Kutta scheme (Wang & Spiteri 2007).

We use the Helmholtz equation of state for modeling the microphysics (Timmes 1999). The equation of state describes the properties of noninteracting electron gas of arbitrarily relativistic and degenerate levels. It also contains a contribution from nuclei as a classical ideal gas, photon gas in the Planck distribution, and electron–positron pair. The Coulomb correction is also included for the screening effects between electron gas and nuclei.

To describe the chemistry, we use the seven-isotope network identical to Timmes & Arnett (1999). This network contains ^{4}He, ^{12}C, ^{16}O, ^{20}Ne, ^{24}Mg, ^{28}Si, and ^{56}Ni. We note that this is the most simplified network one can use to describe the nuclear reaction of CO and ONe matter. However, as all isotopes in this network are along the α-chain network, to accommodate the electron-capture physics, we treat the mean electron mole number Y_e (also known as the electron fraction) as an independent quantity. It follows the fluid motion as a scalar quantity, but it can be modified by including the electron-

capture rate (see below for further discussion). With Y_e as an extra quantity, in the code, we treat the mean atomic number $\bar{Z}$ as the implied value from the mean mass number $\bar{A}$ and Y_e that $\bar{Z} = \bar{A}Y_e$.

Appendix B
Comparison with Literature

B.1. Reinecke et al. (2002a) and Related Works

Our code has a similar structure as Reinecke et al. (2002a) but with some distinctive differences. In Table B1, we tabulate the similarities and differences of our code compared with theirs. In general, the codes are similar, as we make detailed references while validating our code performance.

Our model 300-000-1-c3-1 is similar to their model c3_2d_256 in terms of resolution and initial flame structure. They have a total nuclear reaction energy of 7.19×10^{50} erg and Ni production of 0.40 $M_\odot$. Approximately 0.6 $M_\odot$ of matter is burned. In our model, we have a stronger explosion of 9.69×10^{50} erg released by nuclear reaction and 0.35 $M_\odot$ of ^{56}Ni. Here 0.625 $M_\odot$ of matter is burned by the deflagration. The difference in the choice of equation of state, electron-capture rate, and detailed implementation of subgrid-scale turbulence can contribute to the observed differences. Despite that, we obtain a qualitatively very similar flame structure, as seen from their Figure 2.

B.2. Jones et al. (2016)

This work is based on the extension from Reinecke et al. (2002a) and the later extension in the microphysics, in particular the electron-capture table for the NSE matter, by including rates from, e.g., Nabi & Klapdor-Kleingrothaus (2004). They focused on the deflagration phase of the ONe core in the context of electron-capture SNe evolved from super-AGB stars (Jones et al. 2013).

Their three-dimensional code allows them to explore complex off-center flame structure. Their model G15 is similar to our model 900-000-1-c3-1 (in Appendix C) but differs by flame structure owing to their three-dimensional freedom in flame placement. They observe ejecta and remnant masses of 0.177 and 1.212 $M_\odot$. On the other hand, we observe a larger ejecta mass by 0.567 $M_\odot$. The difference might be originated from the initial flame we use (c3 flame), which is extended in size by $\sim$100 km. This also enhances the energy release by deflagration. Also, its aspherical shape facilitates turbulence production and hence the amount of matter burned at early time. This suppresses the initial electron-capture effect.

B.3. Long et al. (2014)

This code uses another code, FLASH, for modeling the deflagration phase of SNe Ia. Again, we tabulate their input physics in Table B1. The major difference of this code is that the flame propagation does not depend on subgrid-scale turbulence but rather only RT instabilities. Notice that such instabilities depend on local gravity g. Near the core, the local gravity scales as $g(r) \sim m(r)/r^2 \sim \rho r \to 0$. This means that the flame is almost like laminar near the center. On the other hand, there is no such restriction in the subgrid-scale turbulence model. As long as the shear stress is strong, eddy motion can be generated anywhere inside the star, which accelerates the flame propagation.

Long et al. (2014) construct a WD of mass 1.365 $M_\odot$ with equal mass fractions of ^{12}C and ^{16}O. Again, the use of three-dimensional hydrodynamics offers the possibility to explore off-center bubble flame structure.

Due to the weaker flame propagation, they observe a higher bound mass for the same amount of bubbles used when compared with Fink et al. (2014). We notice the drastic difference in the flame structure. While the flame structure strongly affects the explosion energetics in three-dimensional simulations, we only compare with the global trends of their models. We do not compare the ejecta mass because we cannot find the corresponding numbers.

Table B1
Comparison of the Input Physics with Works in the Literature

Physics	This Work	Reinecke et al. (2002a)	Jones et al. (2016)	Long et al. (2014)	Fink et al. (2014)
Hydrodynamics	WENO	Prometheus	Prometheus	FLASH	Prometheus
Dimensionality	2	2	3	3	3
Microphysics	Helmholtz	Private	Private	Helmholtz	Private
E-cap. scheme	Extended	n/a	Extended	n/a	Seitenzahl et al. (2009)
PP isotope no.	495	n/a	384	n/a	384
Tracer no.	160[2]	n/a		10^7	200[3]
Flame cap.	Level-set	Level-set	Level-set	3-step	Level-set
Nuc. network	3-step	Table	Table	3-step	Table
Hyd. isotope no.	7	5	5	3	5
SSG	One-eq. model	One-eq. model	One-eq. model	n/a	One-eq. model

Note. "Hydrodynamics" is the hydrodynamics solver used for solving the Euler equations. "Dimensionality" is the number of dimensions used in the simulations. "Microphysics" is the equation of state used. "E-cap. scheme" is the electron-capture scheme. "PP isotope no." is the number of isotopes used in the postprocessing, and "tracer no." is the number of passive tracers for recording the thermodynamical history. "Flame cap." is the flame capturing scheme used for tracking the deflagration front. "Nuc. network" is the simplified network used in the hydrodynamics simulations, with "3-step" for the three-step nuclear reaction scheme described in Townsley et al. (2002) and "table" for the prebuilt nuclear reaction table. "Hyd. isotope no." is the number of isotopes used in the hydrodynamics simulations. "SSG" is the subgrid-scale turbulence scheme used to model the development of eddy motion. In the table, "n/a" means that no exact implementation details can be found.

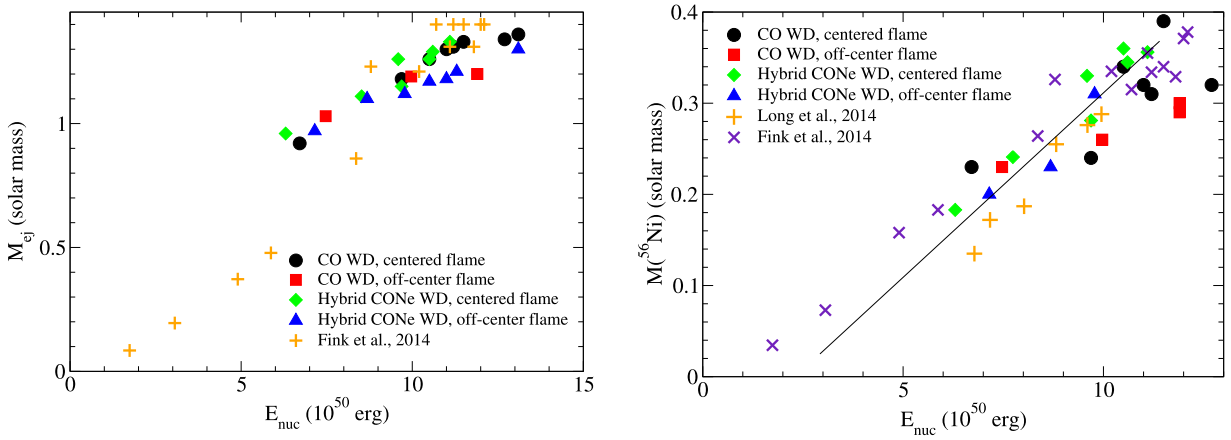

Figure B1. (Left panel) Ejecta mass against total energy released by nuclear reactions computed by our models and in those reported in Fink et al. (2014). (Right panel) Similar to the left panel but for the ^{56}Ni mass against the total energy released by nuclear reactions and also in those reported in Fink et al. (2014) and Long et al. (2014). A fitted straight line is shown to demonstrate the trend of the models.

In the right panel of Figure B1, we plot the ^{56}Ni mass in the ejecta against nuclear energy release of all models. We can see a very consistent trend between our work and their work. This suggests that our code can capture a consistent result in following how the energy input from deflagration contributes to the final ejecta mass. Our models show as narrow band as theirs, which can reach as high as $M_{\rm Ni}$. This means that in the high-mass regime, the faster and stronger nuclear flame is balanced by other effects, such as the electron-capture effects. The production of ^{56}Ni therefore becomes saturated. However, our models do not show that $E_{\rm nuc}$ reaches as low as theirs. Such models will need further exploration of the three-dimensional flame structure where a much smaller initial flame in the form of a few bubbles is used.

B.4. Fink et al. (2014)

Similar to Seitenzahl et al. (2013), Fink et al. (2014) carried out a parameter survey for the PTD for the near-Chandrasekhar mass model in three dimensions. The code structure is inherited from previous versions, such as Reinecke et al. (2002a), but with an updated turbulence calculation described in Schmidt et al. (2006). A wide range of flame structures from one to 1600 bubbles are used to study their effects on the chemical abundance pattern and its observable. The progenitor has a central density of 2.9×10^9 g cm^{-3} and a composition of $X(^{12}\mathrm{C}) = 0.475$, $X(^{16}\mathrm{O}) = 0.5$, and $X(^{22}\mathrm{Ne}) = 0.025$. The ejecta mass increases from $\sim$0.08 $M_\odot$ to complete disruption ($=$1.4 $M_\odot$) when the bubble count exceeds 150.

Since it is difficult to compare models with a different flame structure, we compare the global trends of their models with ours. In their models, they show that the ejecta mass increases almost linearly with the explosion energy. We also plot the explosion energetics of their models in both panels of Figure B1.

In the left panel, we plot the relation between the ejecta mass and the total nuclear energy released. We see a very clear linear trend in our models. Their models also show a similar trend but with lower and higher ends of the ejecta mass. Despite the difference in the range, the slopes, which characterize how the deflagration contributes to the mass ejection, agree with each other in the high-$E_{\rm nuc}$ limit. Furthermore, our models are confined in a narrow bin from the fitted straight line. But we also notice that, for a model with $E_{\rm nuc} < 10^{51}$] erg, their model has a steeper slope than ours. We notice that the diversity of their model depends on the initial flame instead of the progenitor mass. A centered flame like ours provides a sufficiently large surface area to maintain burning before the expansion quenches the deflagration wave. Therefore, our models tend to cluster on the strong explosion side, while in their work, the models span from weak to strong explosions.

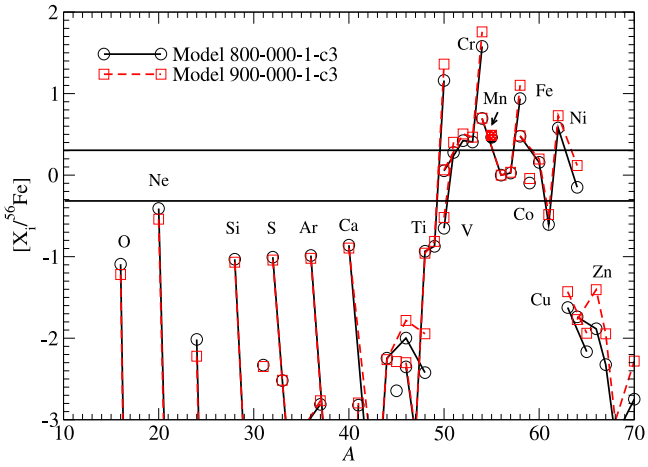

Figure B2. $[X_i/^{56}\mathrm{Fe}]$ against atomic mass for the ejecta of pure ONe WD models for 800-000-1-c3-1 ($\rho_c \approx 10^{9.9}$ g cm^{-3}) and 900-000-1-c3-1 ($\rho_c \approx 10^{9.95}$ g cm^{-3}). All models assume O+Ne+Mg composition with, $X(^{22}\mathrm{Ne}) = 0.025$, and $c3$ initial flame.

In the right panel, we make a similar plot to the left panel but for the ^{56}Ni mass production. Again, the trends among all works show a promising similarity. The models in their work again show the lower ^{56}Ni mass in the lower end. Their models show a similar ^{56}Ni mass in the upper end. The consistency in the slope, as well as the thin band formed by all the models, shows that our code agrees well with their hydrodynamics and postprocess results.

Appendix C
O+Ne+Mg WD

In the main text, we presented a detailed description of how the nucleosynthesis varies with the model parameters of a C+O

Table C1
Mass of Major Isotopes in the Ejecta after All Short-lived Radioactive Isotopes Have Decayed

Isotopes	800-000-1-c3-1	800-000-1-b1-1	900-000-1-c3-1
^{12}C	1.53×10^{-7}	1.29×10^{-7}	1.92×10^{-7}
^{13}C	9.46×10^{-14}	7.52×10^{-14}	9.42×10^{-14}
^{14}N	1.77×10^{-9}	8.72×10^{-10}	1.98×10^{-9}
^{15}N	3.6×10^{-7}	1.40×10^{-7}	3.27×10^{-7}
^{16}O	2.56×10^{-1}	1.37×10^{-1}	1.96×10^{-1}
^{17}O	4.86×10^{-12}	1.82×10^{-12}	1.20×10^{-12}
^{18}O	3.62×10^{-14}	1.78×10^{-14}	2.80×10^{-14}
^{19}F	2.18×10^{-12}	1.12×10^{-12}	1.5×10^{-12}
^{20}Ne	1.93×10^{-1}	1.5×10^{-1}	1.46×10^{-1}
^{21}Ne	1.72×10^{-8}	7.44×10^{-9}	7.44×10^{-9}
^{22}Ne	4.72×10^{-8}	2.83×10^{-8}	2.65×10^{-8}
^{23}Na	3.53×10^{-8}	1.56×10^{-8}	1.68×10^{-8}
^{24}Mg	2.8×10^{-3}	9.22×10^{-4}	1.32×10^{-3}
^{25}Mg	4.53×10^{-9}	1.99×10^{-9}	2.3×10^{-9}
^{26}Mg	8.90×10^{-9}	6.26×10^{-9}	6.19×10^{-9}
^{26}Al	3.38×10^{-29}	5.29×10^{-13}	5.21×10^{-13}
^{27}Al	1.90×10^{-6}	7.24×10^{-7}	1.26×10^{-6}
^{28}Si	2.58×10^{-2}	2.7×10^{-2}	2.43×10^{-2}
^{29}Si	6.14×10^{-6}	3.46×10^{-6}	6.32×10^{-6}
^{30}Si	2.66×10^{-6}	1.74×10^{-6}	3.15×10^{-6}
^{31}P	1.1×10^{-5}	6.8×10^{-6}	9.98×10^{-6}
^{32}S	1.61×10^{-2}	1.36×10^{-2}	1.52×10^{-2}
^{33}S	4.8×10^{-6}	2.35×10^{-6}	4.21×10^{-6}
^{34}S	9.9×10^{-7}	9.7×10^{-7}	1.19×10^{-6}
^{36}S	2.30×10^{-10}	1.11×10^{-9}	3.48×10^{-10}
^{35}Cl	9.93×10^{-7}	7.87×10^{-7}	9.92×10^{-7}
^{37}Cl	7.12×10^{-7}	4.97×10^{-7}	8.9×10^{-7}
^{36}Ar	3.57×10^{-3}	3.4×10^{-3}	3.38×10^{-3}
^{38}Ar	4.60×10^{-7}	3.56×10^{-7}	4.17×10^{-7}
^{40}Ar	2.45×10^{-11}	1.1×10^{-10}	3.61×10^{-11}
^{39}K	4.86×10^{-7}	3.54×10^{-7}	4.84×10^{-7}
^{40}K	9.60×10^{-13}	1.42×10^{-12}	1.34×10^{-12}
^{41}K	1.60×10^{-7}	1.20×10^{-7}	1.75×10^{-7}
^{40}Ca	3.61×10^{-3}	3.4×10^{-3}	3.41×10^{-3}
^{42}Ca	4.74×10^{-8}	5.78×10^{-7}	1.82×10^{-7}
^{43}Ca	3.68×10^{-9}	2.10×10^{-8}	5.77×10^{-9}
^{44}Ca	3.47×10^{-6}	3.0×10^{-6}	3.41×10^{-6}
^{46}Ca	1.2×10^{-8}	7.39×10^{-8}	1.72×10^{-8}
^{48}Ca	2.26×10^{-7}	1.13×10^{-5}	6.94×10^{-7}
^{45}Sc	3.39×10^{-8}	1.5×10^{-7}	7.95×10^{-8}
^{46}Ti	4.18×10^{-7}	5.7×10^{-7}	4.83×10^{-7}
^{47}Ti	5.76×10^{-8}	8.28×10^{-8}	6.37×10^{-8}
^{48}Ti	1.6×10^{-4}	9.43×10^{-5}	1.3×10^{-4}
^{49}Ti	9.34×10^{-6}	2.47×10^{-5}	1.9×10^{-5}
^{50}Ti	9.98×10^{-4}	6.66×10^{-3}	1.62×10^{-3}
^{50}V	7.33×10^{-8}	1.73×10^{-7}	1.1×10^{-7}
^{51}V	2.63×10^{-4}	8.73×10^{-4}	3.59×10^{-4}

Note. The isotope masses are in units of solar mass.

Table C2
(cont'd) Mass of Major Isotopes in the Ejecta after All Short-lived Radioactive Isotopes Have Decayed

Isotopes	800-000-1-c3-1	800-000-1-b1-1	900-000-1-c3-1
^{50}Cr	3.33×10^{-4}	3.69×10^{-4}	3.50×10^{-4}
^{52}Cr	1.57×10^{-2}	2.82×10^{-2}	1.94×10^{-2}
^{53}Cr	1.76×10^{-3}	3.11×10^{-3}	2.6×10^{-3}
^{54}Cr	6.65×10^{-3}	3.59×10^{-2}	1.2×10^{-2}
^{55}Mn	1.60×10^{-2}	2.14×10^{-2}	1.74×10^{-2}
^{54}Fe	1.50×10^{-1}	1.60×10^{-1}	1.55×10^{-1}
^{56}Fe	4.97×10^{-1}	5.0×10^{-1}	5.9×10^{-1}
^{57}Fe	1.28×10^{-2}	1.45×10^{-2}	1.34×10^{-2}
^{58}Fe	1.61×10^{-2}	7.12×10^{-2}	2.40×10^{-2}
^{60}Fe	2.38×10^{-6}	4.87×10^{-5}	6.4×10^{-6}
^{59}Co	1.11×10^{-3}	1.89×10^{-3}	1.30×10^{-3}
^{58}Ni	6.6×10^{-2}	6.49×10^{-2}	6.29×10^{-2}
^{60}Ni	1.15×10^{-2}	1.55×10^{-2}	1.30×10^{-2}
^{61}Ni	9.27×10^{-5}	2.89×10^{-4}	1.25×10^{-4}
^{62}Ni	4.41×10^{-3}	1.57×10^{-2}	6.41×10^{-3}
^{64}Ni	2.52×10^{-4}	3.32×10^{-3}	4.77×10^{-4}
^{63}Cu	6.2×10^{-6}	4.41×10^{-5}	9.63×10^{-6}
^{65}Cu	7.99×10^{-7}	7.29×10^{-6}	1.37×10^{-6}
^{64}Zn	7.72×10^{-6}	5.86×10^{-6}	7.32×10^{-6}
^{66}Zn	3.24×10^{-6}	1.37×10^{-4}	1.0×10^{-5}
^{67}Zn	1.75×10^{-7}	3.68×10^{-6}	4.27×10^{-7}
^{68}Zn	1.4×10^{-7}	1.2×10^{-6}	1.68×10^{-7}
^{70}Zn	1.5×10^{-8}	3.42×10^{-7}	3.15×10^{-8}

Note. The isotope masses are in units of solar mass.

Table C3
Masses of the Radioactive Isotopes in the Ejecta after the Explosion

Isotopes	800-000-1-c3-1	800-000-1-b1-1	900-000-1-c3-1
^{22}Na	1.71×10^{-10}	1.27×10^{-10}	1.20×10^{-10}
^{26}Al	2.76×10^{-9}	1.46×10^{-9}	2.58×10^{-9}
^{39}Ar	8.96×10^{-13}	2.43×10^{-12}	1.25×10^{-12}
^{40}K	9.65×10^{-13}	1.43×10^{-12}	1.35×10^{-12}
^{41}Ca	1.54×10^{-7}	1.19×10^{-7}	1.74×10^{-7}
^{44}Ti	3.27×10^{-6}	2.82×10^{-6}	3.22×10^{-6}
^{48}V	5.33×10^{-9}	5.25×10^{-9}	5.40×10^{-9}
^{49}V	2.36×10^{-7}	3.37×10^{-7}	2.82×10^{-7}
^{53}Mn	8.60×10^{-4}	1.12×10^{-3}	9.63×10^{-4}
^{60}Fe	3.40×10^{-5}	6.84×10^{-4}	8.50×10^{-5}
^{56}Co	1.54×10^{-4}	1.72×10^{-4}	1.63×10^{-4}
^{57}Co	2.32×10^{-3}	2.89×10^{-3}	2.50×10^{-3}
^{60}Co	1.82×10^{-6}	7.75×10^{-6}	2.73×10^{-6}
^{56}Ni	3.83×10^{-1}	3.22×10^{-1}	3.70×10^{-1}
^{57}Ni	9.47×10^{-3}	8.72×10^{-3}	9.43×10^{-3}
^{59}Ni	7.38×10^{-4}	9.3×10^{-4}	7.91×10^{-4}
^{63}Ni	4.95×10^{-6}	3.65×10^{-5}	7.92×10^{-6}

Note. The isotope masses are in units of solar mass.

WD and a hybrid C+O+Ne WD. In fact, a super-AGB star with a mass of 8–10 $M_\odot$ can also form a massive O+Ne+Mg WD, where the core or shell O burning is ignited by electron capture can and can trigger the oxygen deflagration.

The outcome of the oxygen deflagration is most sensitive to the central density of the WD when the deflagration is initiated, which is called as the deflagration density $\rho_{\rm c,def}$. This is because electron capture on NSE materials leads to the collapse of the WD, while nuclear energy release by the oxygen deflagration leads to the expansion.

Zha et al. (2019) investigated how $\rho_{\rm c,def}$ depends on the electron capture rate, nuclear reaction rate, URCA process, and convective criterion and concluded $\log_{10}(\rho_{\rm c,def}/{\rm g\,cm^{-3}}) > 10.10$ is most likely. Such high $\rho_{\rm c,def}$ has been found to lead to collapse to form a neutron star rather than thermonuclear explosion (Leung et al. 2020; Zha et al. 2019).

Earlier Jones et al. (2016, 2019) have found the the outcome for $\log_{10}(\rho_{\rm c,def}/{\rm g\ cm^{-3}}) = 9.95$ is thermonuclear explosion that leaves a small mass WD behind, being similar to PTD models presented in the main text.

Although we think the collapse is the likely outcome of oxygen deflagration in the actualy O+Ne+Mg WDs with $\log_{10}(\rho_{\rm c,def}/{\rm g\,cm^{-3}}) > 10.10$, we perform numerical experiments

of the pure oxygen deflagration at lower $\rho_{c,def}$, i.e., $\log_{10}(\rho_{c,def}/\mathrm{g\,cm^{-3}}) = 9.95$ and 9.90 for the purpose of comparisons with Jones et al. (2016) and with the similar $\rho_{c,def}$ as C+O and C+O +Ne WD models.

In this section, we examine the explosive nucleosynthesis of the O+Ne+Mg WD. In Tables C1–C3, we tabulate the nucleosynthesis yield and the radioactive isotopes in the ejecta.

C.1. Ejecta of O+Ne+Mg WD

C.1.1. Dependence on Central Density

Here we compare the nucleosynthesis pattern of O+Ne+Mg WD models of different central densities. For our numerical experiments, we adopt the ρ_c range from $10^{9.90-9.95}\,\mathrm{g\,cm^{-3}}$ (i.e., $8-9\times10^{9}\,\mathrm{g\,cm^{-3}}$). Higher ρ_c in general result in a collapse to form a neutron star.

We compare in Figure B2 the ejecta chemical composition of models 800-000-1-c3-1 and 900-000-1-c3-1. Notice that the typical explosion of the O+Ne+Mg WD is weaker than the C +O counterpart because the nuclear energy release from O+Ne +Mg matter to NSE is smaller than the energy release from C +O matter to NSE. Also, the progenitor is more compact.

The progenitor mass still plays an important role in the ejecta composition for the O+Ne+Mg WD case. The IMEs are still underproduced, and most iron-peak elements are significantly produced. The models show a similar composition, except that the lower-mass one shows a higher yield of ^{50}Ti, $^{50-51}$V, ^{54}Cr, ^{58}Fe, and ^{60,62}Ni. During the fallback of matter in the inner layer, most iron-peak elements, including neutron-rich isotopes, are trapped in the remnant. Also, the higher-density WD is more compact; thus, the inner layer requires a higher escape velocity for mass ejection. As a result, a larger amount of the inner part of matter is trapped, which suppresses the increase in neutron-rich isotopes.

C.1.2. Dependence on Initial Flame Structure

Here we compare the nucleosynthesis yield of the O+Ne+Mg WD models with different initial flames. In Figure C1, we plot $[X_i/^{56}\mathrm{Fe}]$ for models 800-000-1-c3-1 and 800-000-1-b1-1.

The ejecta properties are significantly different when the flame starts from off-center. Major isotopes of iron-peak elements are similar. But the amount of neutron-rich isotopes can be 1–2 orders of magnitude higher for the off-center flame than the centered flame. This is because the outer flame can channel the ash outward at an earlier time, which allows more matter containing neutron-rich isotopes to escape from the gravitational pull of the star. On the other hand, IMEs are only mildly changed. More neutron-rich isotopes are seen in the model with an off-center flame than that with a centered flame.

C.2. Remnant of O+Ne+Mg WD

C.2.1. Dependence on Central Density

We compare the remnant composition for O+Ne+Mg WDs with different ρ_c by comparing models 800-000-1-c3-1 and 900-000-1-c3-1. In Figure C2, we plot $[X_i/^{56}\mathrm{Fe}]$ for these two models. The remnant WD exhibits very peculiar abundance as also seen in the high-density models of C+O and hybrid C+O +Ne WDs, where iron-peak elements can be 10^3 times higher than the solar value. The different central density provides a very different abundance pattern in the remnant WD, in contrast to the lower-mass counterpart. The lower-density model (800-000-1-c3) has much higher neutron-rich isotopes of iron-peak elements than the higher-density model (900-000-1-c3) in the remnant WD. They can be $\sim10^{3-4}$ times higher than the solar ratios. Also, there is no observable amount of IMEs. Meanwhile, model 900-000-1-c3 shows the abundance pattern closer to the solar composition. The IMEs are underproduced at a level of $\sim$10% of the solar values. The most overproduced isotope is ^{54}Cr, and it is only $\sim$100 times higher, which is almost 2 orders of magnitude lower than that in model 800-000-1-c3.

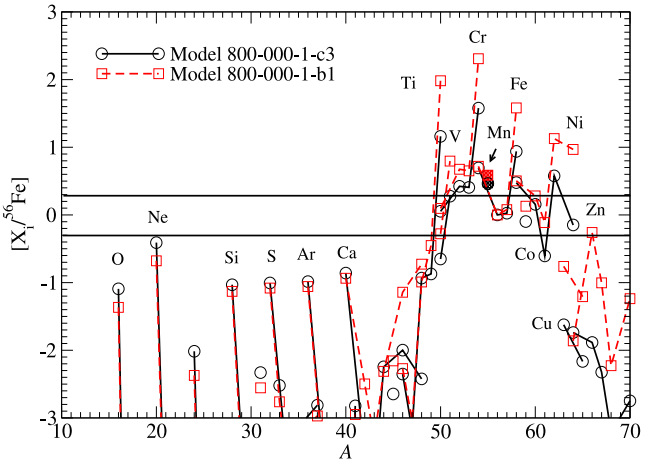

Figure C1. $[X_i/^{56}\mathrm{Fe}]$ against atomic mass for the ejecta of pure ONe WD models for 800-000-1-c3-1 ($c3$ flame) and 800-000-1-b1-1 ($b1$ flame). All models assume $\rho_c = 10^{9.90}\times10^{9}\,\mathrm{g\,cm^{-3}}$, O+Ne+Mg composition, and $X(^{22}\mathrm{Ne}) = 0.025$.

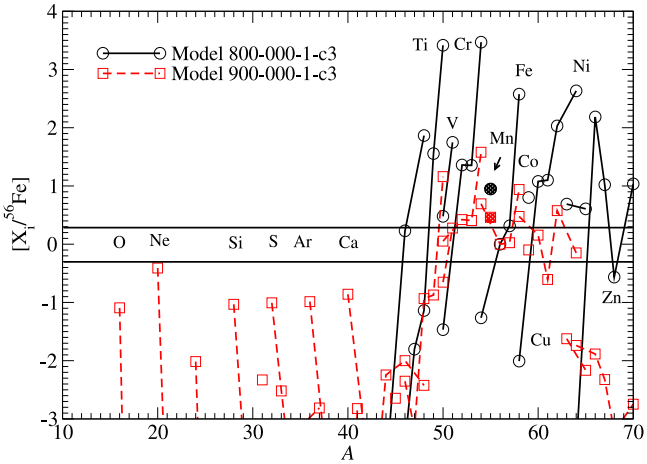

Figure C2. $[X_i/^{56}\mathrm{Fe}]$ against atomic mass for the bounded remnant of pure ONe WD models for models 800-000-1-c3-1 ($\rho_c \approx 10^{9.9}\,\mathrm{g\,cm^{-3}}$) and 900-000-1-c3-1 ($\rho_c \approx 10^{9.95}\,\mathrm{g\,cm^{-3}}$). All models assume O+Ne+Mg composition, $X(^{22}\mathrm{Ne}) = 0.025$, and $c3$ initial flame.

C.2.2. Dependence of Initial Flame Structure

In Figure C3, we compare the abundance pattern for the remnant part of models 800-000-1-c3-1 and 800-000-1-b1-1. The remnant in the centered flame model has no observable O+Ne+Mg-rich matter or IMEs. The overproduction of iron-peak elements, especially neutron-rich isotopes, is similar to the high-density model in C+O and hybrid C+O+Ne WD models. However, the off-center model has more neutron-rich isotopes than the centered flame model. Again, in such a high density, electron capture begins to be important to the global dynamics

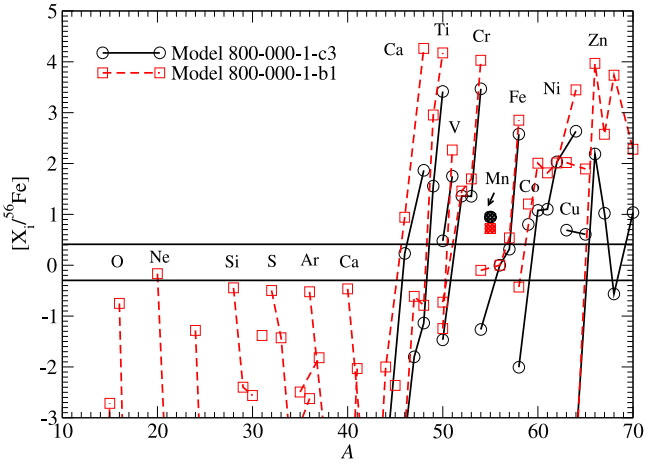

Figure C3. Scaled mass fraction $[X_i/^{56}\mathrm{Fe}]$ against atomic mass for the remnant of pure ONe WD models for 800-000-1-c3-1 ($c3$ flame) and 800-000-1-b1-1 ($b1$ flame). All models assume $\rho_c = 10^{9.90}$ g cm^{-3}, O+Ne+Mg composition, and $X(^{22}\mathrm{Ne}) = 0.025$.

as it suppresses the pressure jump after the matter is burned. The ejecta in the centered flame is more suppressed than the ejecta in the off-center flame.

ORCID iDs

Shing-Chi Leung https://orcid.org/0000-0002-4972-3803
Ken'ichi Nomoto https://orcid.org/0000-0001-9553-0685

References

Asplund, M., Grevesse, N., Sauval, A. J., & Scott, P. 2009, ARA&A, 47, 481
Barth, T. J., & Deconinck, H. 1999, Lecture Notes in Computational Science and Engineering 9: High-Order Methods for Computational Physics (Berlin: Springer)
Bell, J. B., Day, M. S., Rendleman, C. A., Woosley, S. E., & Zingale, M. 2004a, ApJ, 606, 1029
Bell, J. B., Day, M. S., Rendleman, C. A., Woosley, S. E., & Zingale, M. 2004b, ApJ, 608, 883
Benvenuto, O. G., Panei, J. A., Nomoto, K., Kitamura, H., & Hachisu, I. 2015, ApJL, 809, L6
Branch, D., Thomas, R. C., Baron, E., et al. 2004, ApJ, 606, 413
Brooks, J., Schwab, J., Bildsten, L., Quataert, E., & Paxton, B. 2017, ApJL, 834, L9
Brown, W. R., Kilic, M., Allende Prieto, C., & Kenyon, S. J. 2010, ApJ, 723, 1072
Calder, A. C., Townsley, D. M., Seitenzahl, I. R., et al. 2007, ApJ, 656, 313
Cescutti, G., & Kobayashi, C. 2017, A&A, 607, A23
Clement, M. J. 1993, ApJ, 406, 651
Dave, P., Kashyap, R., Fisher, R., et al. 2017, ApJ, 841, 58
Denissenkov, P. A., Herwig, F., Truran, J. W., & Paxton, B. 2013, ApJ, 772, 37
Fink, M., Kromer, M., Seitenzahl, I. R., et al. 2014, MNRAS, 438, 1762
Foley, R. J., Challis, P. J., Chornock, R., et al. 2013, ApJ, 767, 57
Foley, R. J., Chornock, R., Filippenko, A. V., et al. 2009, AJ, 138, 376
Foley, R. J., Pan, Y.-C., Brown, P., et al. 2016, MNRAS, 461, 1308
Gamezo, V. N., Khokhlov, A. M., & Oran, E. S. 2004, PhRvL, 92, 211102
García-Berro, E., & Lorén-Aguilar, P. 2017, in Handbook of Supernovae, ed. A. W. Alsabti & P. Murdin (Cham: Springer), 1237
Hicks, E. P. 2015, ApJ, 803, 72
Hoeflich, P. 2017, in Handbook of Supernovae, ed. A. W. Alsabti & P. Murdin (Cham: Springer), 1151
Iwamoto, K., Brachwitz, F., Nomoto, K., et al. 1999, ApJS, 125, 439
Jackson, A. P., Townsley, D. M., & Calder, A. C. 2014, ApJ, 784, 174
Jha, S. W. 2017, in Handbook of Supernovae, ed. A. W. Alsabti & P. Murdin (Cham: Springer International Publishing AG), 375
Jiang, J.-a., Doi, M., Maeda, K., & Shigeyama, T. 2018, ApJ, 865, 149
Jones, S., Hirschi, R., Nomoto, K., et al. 2013, ApJ, 772, 150
Jones, S., Röpke, F. K., Fryer, C., et al. 2019, A&A, 622, A74
Jones, S., Röpke, F. K., Pakmor, R., et al. 2016, A&A, 593, A72
Jordan, G. C. I., Perets, H. B., Fisher, R. T., et al. 2012, ApJ, 759, 53
Kawabata, M., Kawabata, K., Maeda, K., et al. 2018, PASJ, 70, 111
Kobayashi, C., Leung, S.-C., & Nomoto, K. 2020, ApJ, 895, 138
Kobayashi, C., Nomoto, K., & Hachisu, I. 2015, ApJL, 804, L24
Kromer, M., Fink, M., Stanishev, V., et al. 2013, MNRAS, 429, 2287
Kromer, M., Ohlmann, S. T., Pakmor, R., et al. 2015, MNRAS, 450, 3045
Lecoanet, D., Schwab, J., Quataert, E., et al. 2016, ApJ, 832, 71
Leung, S.-C., Chu, M.-C., & Lin, L.-M. 2015, MNRAS, 454, 1238
Leung, S.-C., & Nomoto, K. 2017a, in 14th International Symposium on Nuclei in the Cosmos (NIC2016), ed. S. Kubono et al., 020506
Leung, S.-C., & Nomoto, K. 2017b, MmSAI, 88, 266
Leung, S.-C., & Nomoto, K. 2018, ApJ, 861, 143
Leung, S.-C., & Nomoto, K. 2019, PASA, 36, e006
Leung, S.-C., & Nomoto, K. 2020, ApJ, 888, 80
Leung, S.-C., Nomoto, K., & Suzuki, T. 2020, ApJ, 889, 34
Leung, S.-C., Zha, S., Chu, M.-C., Lin, L.-M., & Nomoto, K. 2019, ApJ, 884, 9
Li, W., Filippenko, A. V., Chornock, R., et al. 2003, PASP, 115, 453
Li, W., Filippenko, A. V., Treffers, R. R., et al. 2001, ApJ, 546, 734
Livne, E. 1993, ApJL, 406, L17
Livne, E., & Arnett, D. 1993, ApJL, 415, L107
Long, M., Jordan, G. C. I., van Rossum, D. R., et al. 2014, ApJ, 789, 103
Martínez-Rodríguez, H., Badenes, C., Yamaguchi, H., et al. 2017, ApJ, 843, 35
Matteucci, F., & Greggio, L. 1986, A&A, 154, 279
Nabi, J.-U., & Klapdor-Kleingrothaus, H. V. 2004, ADNDT, 88, 237
Niemeyer, J. C., & Hillebrandt, W. 1995, ApJ, 452, 779
Niemeyer, J. C., Hillebrandt, W., & Woosley, S. E. 1995, ApJ, 452, 769
Niemeyer, J. C., & Woosley, S. E. 1997, ApJ, 475, 740
Nomoto, K. 1982a, ApJ, 253, 798
Nomoto, K. 1982b, ApJ, 257, 780
Nomoto, K. 1984, ApJ, 277, 791
Nomoto, K. 1987, ApJ, 322, 206
Nomoto, K., Kobayashi, C., & Tominaga, N. 2013, ARA&A, 51, 457
Nomoto, K., & Leung, S.-C. 2017a, in Handbook of Supernovae, ed. A. W. Alsabti & P. Murdin (Cham: Springer International Publishing AG), 1275
Nomoto, K., & Leung, S.-C. 2017b, in Handbook of Supernovae, ed. A. W. Alsabti & P. Murdin (Cham: Springer International Publishing AG), 483
Nomoto, K., & Leung, S.-C. 2018, SSRv, 214, 67
Nomoto, K., Sugimoto, D., & Neo, S. 1976, Ap&SS, 39, 37
Nomoto, K., Thielemann, F.-K., & Yokoi, K. 1984, ApJ, 286, 644
Osher, S., & Sethian, J. A. 1988, JCoPh, 79, 12
Pagel, B. E. J. 1997, Nucleosynthesis and Chemical Evolution of Galaxies (Cambridge, UK: Cambridge University Press)
Pakmor, R. 2017, in Violent Mergers, ed. A. W. Alsabti & P. Murdin (Cham: Springer), 1257
Perlmutter, S., Gabi, S., Goldhaber, G., et al. 1997, ApJ, 483, 565
Phillips, M. M. 1993, ApJL, 413, L105
Phillips, M. M., Li, W., Frieman, J. A., et al. 2007, PASP, 119, 360
Pocheau, A. 1994, PhRvE, 49, 1109
Raddi, R., Hollands, M. A., Koester, D., et al. 2018, ApJ, 858, 3
Raddi, R., Hollands, M. A., Koester, D., et al. 2019, MNRAS, 489, 1489
Reinecke, M., Hillebrandt, W., & Niemeyer, J. C. 1999a, A&A, 347, 739
Reinecke, M., Hillebrandt, W., & Niemeyer, J. C. 2002a, A&A, 386, 936
Reinecke, M., Hillebrandt, W., & Niemeyer, J. C. 2002b, A&A, 391, 1167
Reinecke, M., Hillebrandt, W., Niemeyer, J. C., Klein, R., & Gloebl, A. 1999b, A&A, 347, 724
Riess, A. G., Press, W. H., & Kirshner, R. P. 1996, ApJ, 473, 88
Röpke, F. K. 2005, A&A, 432, 969
Röpke, F. K. 2017, in Handbook of Supernovae, ed. A. W. Alsabti & P. Murdin (Cham: Springer), 1185
Röpke, F. K., Gieseler, M., Reinecke, M., Travaglio, C., & Hillebrandt, W. 2006a, A&A, 453, 203
Röpke, F. K., & Hillebrandt, W. 2005, A&A, 431, 635
Röpke, F. K., Hillebrandt, W., & Niemeyer, J. C. 2004a, A&A, 421, 411
Röpke, F. K., Hillebrandt, W., & Niemeyer, J. C. 2004b, A&A, 421, 783
Röpke, F. K., Hillebrandt, W., Niemeyer, J. C., & Woosley, S. E. 2006b, A&A, 448, 1
Röpke, F. K., Hillebrandt, W., Schmidt, W., et al. 2007, ApJ, 668, 1132
Sahu, D. K., Tanaka, M., Anupama, G. C., et al. 2008, ApJ, 680, 580
Schmidt, W., Niemeyer, J. C., Hillebrndt, W., & Roepke, F. K. 2006, A&A, 450, 283

Seitenzahl, I. R., Ciaraldi-Schoolmann, F., Röpke, F. K., et al. 2013, MNRAS, 429, 1156
Seitenzahl, I. R., Taubenberger, S., & Sim, S. A. 2009, MNRAS, 400, 531
Suzuki, T., Zha, S., Leung, S.-C., & Nomoto, K. 2019, ApJ, 881, 64
Taubenberger, S. 2017, in Handbook of Supernovae, ed. A. W. Alsabti & P. Murdin (Cham: Springer International Publishing AG), 317
Timmes, F. X. 1992, ApJL, 423, L131
Timmes, F. X. 1999, ApJ, 124, 241
Timmes, F. X., & Arnett, D. 1999, ApJ, 125, 277
Timmes, F. X., Hoofman, R. D., & Woosley, S. E. 2000, ApJS, 129, 377
Timmes, F. X., & Woosley, S. E. 1992, ApJ, 396, 649
Townsley, D. M., Calder, A. M., Asida, S. M., et al. 2002, ApJS, 143, 201
Townsley, D. M., Miles, B. J., Timmes, F. X., Calder, A. C., & Brown, E. F. 2016, ApJS, 225, 3
Travaglio, C., Hillebrandt, W., Reinecke, M., et al. 2004, ApJ, 425, 1029
Tsuruta, S., Leung, S.-C., & Nomoto, K. 2018, IJMPD, 27, 1830004
Wang, R., & Spiteri, R. J. 2007, SJNA, 45, 1871
Woosley, S. E. 1997, ApJ, 476, 801
Yamaguchi, H., Badenes, C., Foster, A. R., et al. 2015, ApJL, 801, L31
Zha, S., Leung, S.-C., Suzuki, T., & Nomoto, K. 2019, ApJ, 886, 22